PROCESSING AND PROPERTY ENGINEERING OF DOMAINS AND DOMAIN WALLS IN HEXAGONAL MANGANITES

Master Thesis

Submitted by
Max Haas

at

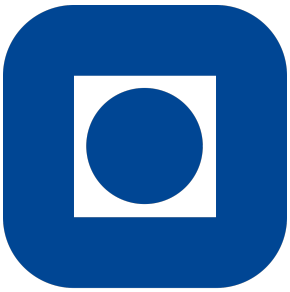

NTNU

Faculty of Natural Sciences
Department of Physics

1. Supervisor Prof. Dr. Jeroen Danon
2. Supervisor Prof. Dr. Dennis Meier

Trondheim, 2022

Abstract

Topologically protected objects have drawn attention in many research areas. From quantum bits to skyrmions, from superfluid helium to the early universe, topology plays a crucial role. It is not always easy to produce or characterize the desired defects and often very special conditions are required. Not so in hexagonal $ErMnO_3$, which displays a ferroelectric domain structure at room temperature, which by nature contains one dimensional topological defects, so called vortex cores. $ErMnO_3$ has a Curie temperature of $T_C = 1156$℃, which allows to study the phase transition from the paraelectric to the ferroelectric phase and therefore the formation of the vortex cores in the laboratory. This gives the chance to study the Kibble-Zurek mechanism, which predicts that the number of vortex cores that can be found in the material depends on the cooling rate at which it transitions T_C.

The goal of this thesis is to investigate the influence of limited system size on the formation of topological defects according to the Kibble-Zurek mechanism by means of a cooling rate experiment using polycrystalline $ErMnO_3$. For this experiment four samples are heated to 1472 °C and cooled over T_C with different cooling rates, i.e. 10^{-2} K/min, 10^{-1} K/min, 10^{0} K/min and 10^{1} K/min. The analysis of the domain structure shows that not only vortex-like domains are present in the individual grains, but also stripe-like domains. It is proposed, that those stripe-like domains are caused by intergranular strain fields, which interact with the vortex cores. Nonetheless an increase in vortex density with increasing cooling rate can be found that can not be explained by strain fields and is therefore assumed to originate in the Kibble-Zurek mechanism. The Kibble-Zurek exponent is significantly lowered from $K = 0.49$ in the single crystal to $K = 0.13$ in the polycrystal. This change can be attributed to effects that are not present in single crystals, such as strain fields, grain boundaries and limited system size.

Sammendrag

Topologisk beskyttede objekter har vakt oppmerksomhet innen mange forskningsområder. Fra kvantebiter til skyrmioner, fra superflytende helium til det tidlige universet, topologi spiller en avgjørende rolle. Det er ikke alltid lett å produsere eller karakterisere de ønskede defektene og ofte kreves det helt spesielle forhold. Ikke så i sekskantet $ErMnO_3$, som vises en ferroelektrisk domenestruktur ved romtemperatur, som av natur inneholder en dimensjonale topologiske defekter, såkalte virvelkjerner. $ErMnO_3$ har en Curie-temperatur av $T_C = 1156℃$, som gjør det mulig å studere faseovergangen fra paraelektrisk til ferroelektrisk fase og derfor dannelsen av virvelkjernene i laboratoriet. Dette gir sjansen til å studere Kibble-Zurek-mekanismen, som forutsier at antall virvelkjerner som kan finnes i materialet avhenger av kjølehastigheten der den går over T_C. Målet med denne oppgaven er å undersøke påvirkningen av begrenset systemstørrelse på for- mating av topologiske defekter i henhold til Kibble-Zurek-mekanismen ved hjelp av en kjølehastighetseksperiment ved bruk av polykrystallinsk $ErMnO_3$. For dette eksperimentet fire prøver varmes opp til 1472 °C og avkjøles over T_C med forskjellige kjølehastigheter, dvs. 10^{-2} K/min, 10^{-1} K/min, 10^{0} K/min og 10^{1} K/min. Analysen av domenestrukturen viser at ikke bare virvellignende domener er tilstede i de enkelte kornene, men også stripe- som domener. Det foreslås at disse stripelignende domenene er forårsaket av intergranulære tøyningsfelt, som samhandler med virvelkjernene. Ikke desto mindre en økning i virvel tetthet med økende kjølehastighet kan bli funnet som ikke kan forklares med belastning felt og antas derfor å stamme fra Kibble-Zurek-mekanismen. The Kibble- Zurek-eksponenten er betydelig senket fra $K = 0.49$ i enkeltkrystallen til $K = 0.13$ i polykrystallen. Denne endringen kan tilskrives effekter som ikke er til stede i single krystaller, som stammefelt, korngrenser og begrenset systemstørrelse.

Contents

Preface

This work was written as the final part of my Masters degree in physics conducted at the Norwegian University of Science and Technology (NTNU) in Trondheim in October 2022. The work has been carried out in the Functional Materials and Materials Chemistry group (FACET) with Prof. Jeroen Danon as my main supervisor and Prof. Dennis Meier as my co-supervisor. This Masters Thesis is my own work, the sample preparations, measurements, analysis and writing was done by my own hand.

I want to thank my supervisors Jeroen and Dennis, especially for the organization and guidance at the start of my thesis and for sorting out the funding to make this work possible. I also want to thank Dr. Jan Schultheiß for investing his time into teaching me the essentials I needed for my lab work as well as revising my thesis and presentations countless times. I also want to thank Ivan Ushakov for his help and instructions on the microscopes.

Max Haas

Trondheim, October 15, 2022

1. Introduction

1.1. Motivation

Since its discovery in 1920 by Joseph Valasek [1, 2], ferroelectric materials have become more and more a center of attention of research groups around the globe. Ferroelectric materials are dielectric insulators that exhibit a spontaneous polarization that can be switched by an external electric field. This property makes them very versatile materials that are of great interest for a wide variety of future applications, from the production of hydrogen [3] to nanoelectronics [4, 5]. They are also the backbone of many every-day applications such as ferroelectric capacitors [6] and actuators [7].

Ferroelectric materials often display a structure that is separated into domains of different polarization states that meet in domain walls. What the structure of the domains and the domain walls looks like varies a lot between different materials and the domains can range from stripe-like configurations and fishbone-like configurations as found in for example $BaTiO_3$ [8] and bubble domains in thin films [9], to vortex-like formations as can be found in hexagonal manganites [10, 11]. But even within one material there are countless methods to engineer the domains in size and shape.

The model material for this work is hexagonal $ErMnO_3$, a material that is known to exhibit a vortex-like domain structure. In this type of structure the domain walls are meandering through the material in an isotropic fashion and meet in one-dimensional topological defects, the so called vortex cores.

More explicitly it is not a single crystal of $ErMnO_3$ that is studied as has extensively been done in the past, but rather polycrystalline samples. The production of polycrystalline manganites has only recently been achieved and their domain structure has not yet been researched until this year by Schultheiß et al. [12]. Polycrystalline materials differ in mainly one big factor from their monocrystalline counterparts, namely a limited system size. Where in a single crystal the system can be viewed as effectively infinite, in a polycrystal the system size is limited by the grain boundaries. Additionally, intergranular strain fields have been shown to effect the domain structure [12].

This work will focus on the effect of a limited system size on the formation of topological defects according to the Kibble-Zurek mechanism in the model system of polycrystalline

$ErMnO_3$. Because of the general nature of the Kibble-Zurek mechanism, the results of this work are not only relevant for domain engineering in the ferroelectric community, but also for other systems that display this defect formation mechanism, i.e. the formation of the early universe [13–15], superfluid helium [16, 17] or colloidal systems [18].

1.2. Outline

This work is divided into 6 chapters, the first one being the introduction to the topic of the domain structure in polycrystalline $ErMnO_3$ and to why it is relevant for the study of both ferroelectric materials and topological defects.
In the second one, the theoretical basis is constructed. The groundwork is laid by explaining how ferroelectricity can arise and by introducing the model system $ErMnO_3$ that is the focus of this work. Its domain structure will be discussed and explained by means of Landau theory and a short excursion into topology and the Kibble-Zurek mechanism. Furthermore the measuring tool that is existential to obtain the data for this work, piezoresponse force microscopy (PFM) is introduced to the reader.
The third chapter of the work explains in detail, how the actual experiment was conducted. It gives detailed insights in the tools that were used, both in the lab and for analysis. It will cover how the samples were prepared, at which parameters the microscope was operated and also how the relevant data was obtained from the images.
In the fourth chapter, the results from the experiment are presented. The PFM images are analyzed for grain size, vortex density and frequency of stripe-like domains in order to characterize the domain structure in the different samples.
Part five provides an extensive discussion of the results shown in chapter 4. The effect of limited system size on the formation of topological defects is addressed as well as how intergranular strain fields may play a role in the formation process of the ferroelectric domains.
Finally the sixth chapter summarizes the results of this work and gives a brief outlook on experiments that could be promising to conduct in the future.

2. Theoretical background

2.1. Ferroelectricity

2.1.1. Definitions

Polarization and surface charge

The polarization P of a material describes a charge separation inside the material. In a dielectric material, which by definition is an electrical insulator, it is caused by an external electric field E, which moves the charges apart following

$$P_i = \chi_{ij} E_j \tag{2.1}$$

where the dielectric susceptibility χ_{ij} is a second-rank tensor [19]. Indices denote the spacial coordinates x, y, z and Einstein's sum convention is used in the following.
The total surface charge density D can then be defined as

$$D_i = \epsilon_0 E_i + P_i \tag{2.2}$$

where $\epsilon = 8.85 \times 10^{-12}\,\mathrm{F\,m^{-1}}$ is the dielectric permittivity of vacuum. It follows that

$$\begin{aligned} D_i &= \epsilon_0 E_i + \chi_{ij} E_j \\ &= \epsilon_0 \delta_{ij} E_j + \chi_{ij} E_j \\ &= \left(\epsilon_0 \delta_{ij} + \chi_{ij}\right) E_j \\ &= \epsilon_{ij} E_j \end{aligned}$$

where

$$\epsilon_{ij} = \epsilon_0 \delta_{ij} + \chi_{ij} \tag{2.3}$$

is the dielectric permittivity of the material. More oftenly reported than ϵ_{ij} is the dielectric constant of a material $\kappa_{ij} = \epsilon_{ij}/\epsilon_0$.

Stress and strain

The relation between the stress X_{ij} applied to a material and the resulting strain x_{ij} can be expressed by Hooke's law

$$x_{ij} = s_{ijkl} X_{kl} \tag{2.4}$$

where the fourth rank tensor s_{ijkl} is called the elastic compliance. The opposite relation can be formulated as

$$X_{ij} = c_{ijkl} x_{kl} \tag{2.5}$$

and in this case the tensor c_{ijkl} is called the stiffness tensor. In some materials, external stress can lead to surface charge density. This effect is called the direct piezoelectric effect and is described by

$$D_i = d_{ijk} X_{jk} \tag{2.6}$$

with the third-rank tensor of the piezoelectric coefficients d_{ijk}. The opposite relation

$$x_{ij} = d_{kij} E_k = d^t_{ijk} E_k \tag{2.7}$$

is then also true, which is called the converse piezoelectric effect. Materials exhibiting these effects are called piezoelectric materials. d^t_{ijk} is the transposed matrix of d_{ijk} It can be shown [20] that all piezoelectric coefficients are 0 for all 11 centrosymmetric point groups as well as for non-centrosymmetric point group 432, because they prohibit odd-rank tensors such as the piezoelectric tensor. This means, that none of the materials in these groups can display any piezoelectric effect.

Pyroelectricity and ferroelectricity

Some materials can exhibit a polarization even without an applied electrical field. This is then referred to as spontaneous polarization P_s [19]. If P_s is caused by a temperature change, the effect is called pyroelectric effect, which is expressed by the equation

$$p_i = \frac{\partial P_{s,i}}{\partial T} \tag{2.8}$$

where T denotes the temperature and p_i is the vector of pyroelectric coefficients. D can therefore be expressed in dependence of the temperature change ΔT

$$D_i = \Delta P_{s,i} = p_i \Delta T \tag{2.9}$$

This spontaneous polarization is only possible in materials that have a unique polar axis. These materials all belong to 10 point groups, which are a subset of the non-centrosymmetric point groups. Therefore all pyroelectric materials are also piezoelectric. Note that the opposite is not true: not all piezoelectric materials are also pyroelectric. Additionally it is possible, that P_s can be switched by applying an external electrical field. Materials that show this behavior are called ferroelectric [19]. This in turn means that all ferroelectric materials are pyroelectric and therefore also piezoelectric, while not all pyroelectric materials are also ferroelectric.
Materials that exhibit only two polarization states with opposite directions are called uniaxial ferroelectrics.

2.1.2. Phase transition and Landau theory

The properties of ferroelectric materials can be derived using Landau theory [21]. Assume the free energy f of a system, that breaks symmetry below a phase transition to be

$$f = f_0 + \frac{1}{2}\alpha\eta^2 + \frac{1}{4}\beta\eta^4 + \dots \tag{2.10}$$

where η is the order parameter of the system. As the phase transition from the paraelectric to the ferroelectric phase occurs at the Curie temperature T_C we can write

$$\alpha = \alpha_0(T - T_C) \tag{2.11}$$

The phase transition is of first order if $\beta < 0$ and of second order for $\beta > 0$ [22]. In this work only the case of $\beta > 0$ is relevant as the model system undergoes a second order phase transition.
The stable states of the system, found by minimizing the free energy, are therefore setting the conditions

$$\frac{\partial f}{\partial \eta} = 0 = \alpha_0(T - T_C)\eta + \beta\eta^3 \tag{2.12}$$

$$\frac{\partial^2 f}{\partial \eta^2} > 0 \tag{2.13}$$

For $T > T_C$ these are fulfilled for $\eta_0 = 0$, resulting in a single minimum. For $T < T_C$ $\eta_0 = 0$ gives a local maximum, the two minima are found at

$$\eta_0 = \pm\sqrt{\frac{\alpha_0}{\beta}(T_C - T)} \sim |T - T_C|^{\frac{1}{2}} = |T - T_C|^{\nu} \tag{2.14}$$

The exponent $\nu = \frac{1}{2}$ is called the critical exponent. Its value can also be derived using molecular field theories [22], which yield the same result. This behavior is demonstrated in Fig. 2.1.

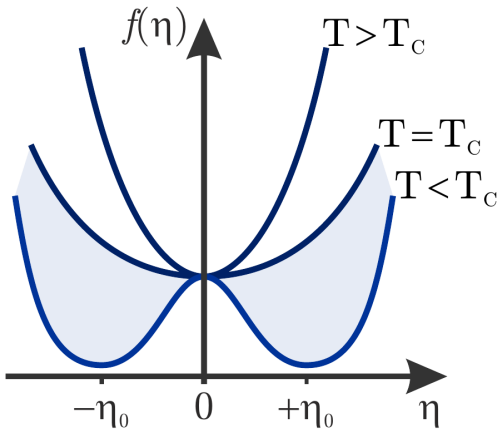

Fig. 2.1.: Free energy over a second order phase transition with order parameter η. Above T_C the function has only one minimum at $\eta = 0$, while below it has two minima at $\eta = \pm\eta_0$ [23].

For some ferroelectrics the order parameter η is the polarization. These materials are called proper ferroelectrics.

Improper ferroelectrics

A ferroelectric material in which the polarization P is not the primary order parameter is called an improper ferroelectric. In this case there exists another order parameter η that is predominant such as structural distortion or charge and the polarization is only secondary. In this case the free energy f needs to be expressed in terms of both order parameters and takes the form [24]

$$f = f_0 + \frac{1}{2}\alpha_0(T - T_C)(\eta_1^2 + \eta_2^2) + \ldots - a(\eta_1^2 - \eta_2^2)P + bP^2 \tag{2.15}$$

Here the primary order parameter $\eta = (\eta_1, \eta_2)$ consists of two components as explained by Cowley et al. [25]. The equilibrium state for the primary order parameter can again be found in two states at $\pm\eta_0 = (\pm\eta_{1,0}, 0)$ [24] and it scales with the square root of the temperature difference.

$$\eta_{1,0} \propto |T - T_C|^{\frac{1}{2}} \tag{2.16}$$

For temperatures above T_C, the free energy is therefore again a single well potential, while below T_C it changes to double well potential with position $\pm P_S$ and depends therefore on the secondary order parameter. Since P couples quadratically to η ($P \propto \eta_1^2 + \eta_2^2$), the temperature scaling of P is now linear.

$$P_s \propto |T - T_C| \tag{2.17}$$

2.1.3. Domain structure

After undergoing the phase transition from a paraelectric to a ferroelectric phase, a spontaneous polarization arises and with it a surface charge. This surface charge then in turn produces an electric field called the depolarizing field E_d, which is oriented opposite P_S. Because upholding an electric field is energetically unfavorable, the material does not fall into a state of a single polarization, but forms so called domains. Inside each domain, the polarization direction is the same, but it points in a different direction than the neighboring domain's polarization. In a material that has only one polarization axis, which means that the polarization between domains must change by 180°. In other materials with multiple polarization axes, for example $BaTiO_3$, other angles are also possible, e.g, 90°. These domains of different polarization states are randomly distributed throughout the material in a way that the net polarization of the whole sample amounts to 0. The area where two domains meet is called a domain wall.
Of course upholding a domain wall comes at its own energy cost, because of the coupling of the microscopic polarization states. From a microscopic perspective it is favorable to have all polarization states pointing the same direction. This energy cost balances the desire of the having an overall polarization of zero, the domains therefore do not become as small as one unit cell as discussed in ref. [26].

2.1.4. Ferroelecric hysteresis

When a small external electric field E is applied to a ferroelectric material, the polarization P increases linearly with the field in accordance with eq. (2.1). Fig. 2.2 shows

this, starting from the origin and following the loop with increasing field. As E becomes stronger, domains in the material that opposed the field begin to flip. This leads to a steep increase of P that is highly nonlinear, eq. (2.1) is not valid anymore. When all domains have aligned with E, the increase of P is linear once more.

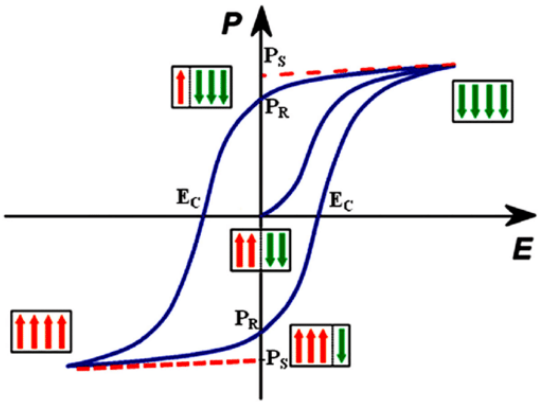

Fig. 2.2.: Ferroelectric hysteresis loop [27] where P_R is the remanent polarization and E_C the coercive field. The dashed red line shows the extrapolation of the linear regime where the polarization is saturated. It's intersection with the polarization axis is the spontaneous polarization P_s

If now E is decreased, P also begins to decrease, but when $E = 0$, P will keep a non-zero value. This nonzero polarization is called the remanent polarization, P_R. To decrease P further, E needs to be inverted to its original direction. The field required to reach $P = 0$ is called the coercive field, E_C. From this point E can be decreased further until P saturates again. In an optimal scenario, the hysteresis loop is perfectly symmetric.
The spontaneous polarization is usually defined as the intersection of the polarization axis with the extrapolation of the linear regime of the saturated polarization (indicated by the dashed lines in Fig. 2.2).

2.2. Hexagonal rare-earth manganites

Rare earth manganites $R\mathrm{MnO_3}$ are a group of improper ferroelectrics that can be divided in two subgroups depending on the crystal structure they form. While the compounds with large R^{3+}-ions (R =Y, Sc, La-Lu) form an orthorhombic structure, the ones with smaller ions (R=Sc, Y, In, Dy – Lu) crystallize to a hexagonal shape [28].

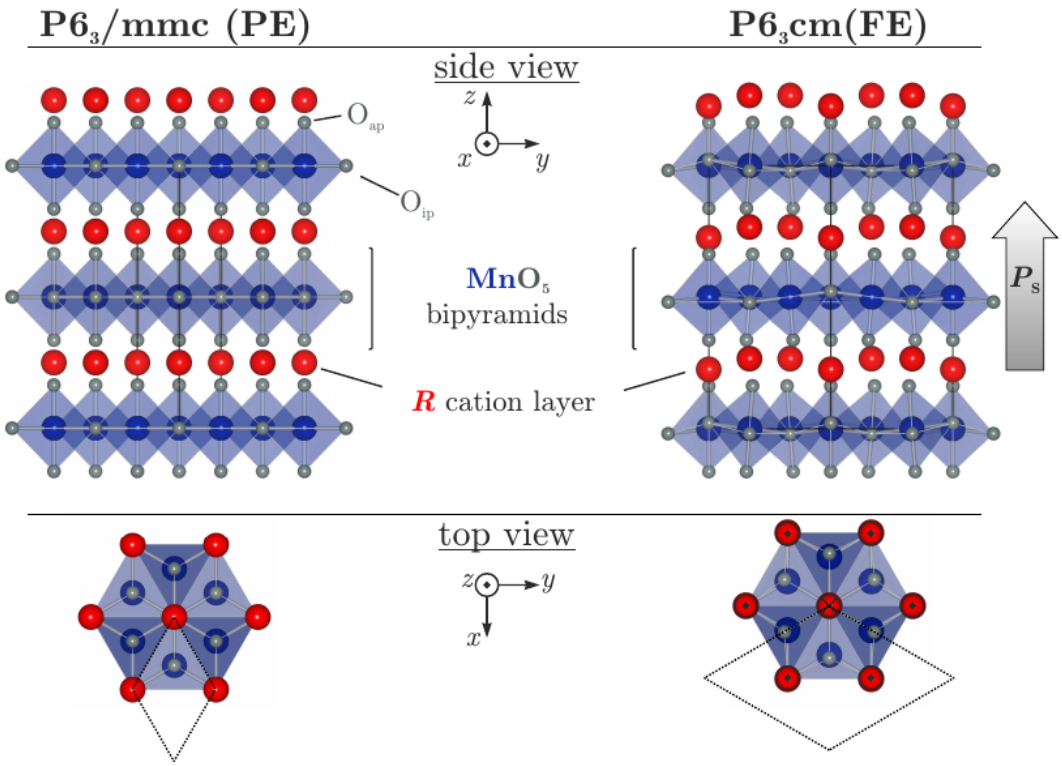

Fig. 2.3.: Crystal structure of hexagonal manganites above (left) and below the Curie temperature T_C (right). Above T_C the MnO_5 bipyramids and the R^{3+} cations are structured in even layers resulting in paraelectric properties. Below T_C the bipyramids are tilted, pushing the cations out of the even plain and into an up-up-down formation. This structural shift induces a polarization along the z-axis and therefore ferroelectric properties emerge in the material [29]. Image taken from [23].

Fig. 2.3 shows the crystal structure of $R\mathrm{MnO_3}$ above and below T_C, which consists of layers of MnO_5 bipyramids interspersed with layers of R^{3+}-ions. Above T_C, both these layers are evenly aligned in the xy-plane and the material is therefore paraelectric. After undergoing the phase transition through T_C, the bipyramids become tilted in a way that they either point towards or away from a central cation. The cations themselves do not stay in an even plain either, but arrange in an up-up-down formation. This dislocation of the charged ions leads to a net polarization P_s in the z-direction of the material. Using the same reasoning, a down-down-up formation is also possible, resulting in the opposite polarization $-P_s$. These are the two possible polarization states for hexagonal manganites that can be found in the domains, it is therefore uniaxial [29].

2.2.1. Topology

The high temperature phase of rare-earth manganites has a $P6_3/mmc$ space group, which is centrosymmetric [30]. As the system undergoes the phase transition at T_C and the bipyramids are tilted as shown in Fig. 2.3, this symmetry is broken. Landau theory [31] and first-principles calculations [32] show that for small amplitudes the energy lowering is independent of the tilt angle. This implies that close to the phase transition the symmetry of the system is a continuous rotational symmetry $U(1)$, which resembles a Mexican hat potential as shown in Fig. 2.4. This means that the free energy can be expressed in polar coordinates in terms of an amplitude Q and a phase Φ.

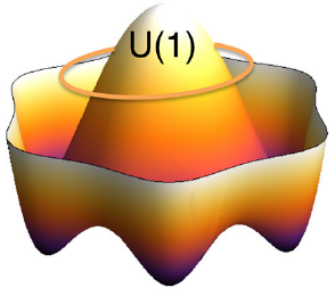

Fig. 2.4.: Mexican hat potential below T_C. Close to T_C the broken symmetry is a $U(1)$ rotational symmetry where all tilt angles of the perovskites have the same energy. The topological defects appearing in such a system are 1D vortices. As the temperature is lowered further, six discrete tilt angles have the most favored energy, corresponding to a Z_6 symmetry [30].

Mapping the space group $U(1)$ to its topological space, the 1D circle S^1, the topological defects occurring in the system can be found. The homotopy tables in [33] show that the expected defects are one-dimensional vortices.
As the system temperature is reduced even further, the tilt angles no longer are continuous, but a few angles have a favored energy state. These are at angles of 0, $2\pi/3$ and $4\pi/3$, which is described by a Z_3 symmetry. These three tilts are denoted by an index α, β and γ respectively. As they can tilt inwards or outwards, this adds another degree of freedom of Z_2 symmetry (denoted by a + or - sign in the index) such that the total symmetry can be described as $Z_2 \times Z_3 = Z_6$. The inward/outward tilt determines the sign of the polarization state, so if the resulting domain is in a $+P$ or $-P$ state. This locking into discrete states leads to a discretized vortex core that is surrounded by six domains of alternating polarization as shown in Fig. 2.5

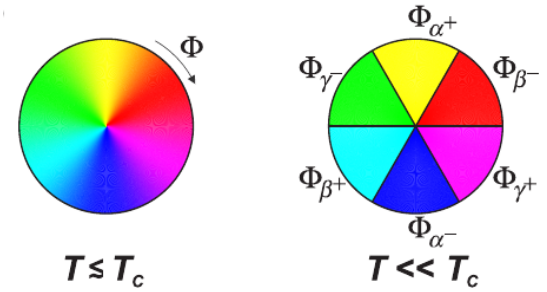

Fig. 2.5.: Close to T_C the phase Φ is continuous, while for lower temperatures it is discretized into six so called clover-leaf domains. The tilt angles have three possible values 0, $2\pi/3$ or $4\pi/3$ denoted by the index α, β and γ. They can also tilt inwards or outwards, denoted by a + or - sign. These six domain states meet in a disrcetized vortex core [10].

Fig. 2.6 shows a PFM scan of monocrystalline $ErMnO_3$ where blue and yellow signify opposite piezoresponse signals and therefore domains of $+P$ and $-P$ polarization. Those domains meet either in domain walls that separate a $+P$ domain from a $-P$ domain by a sharp line or in a discretized vortex core of sixfold symmetry as sketched in Fig. 2.5.

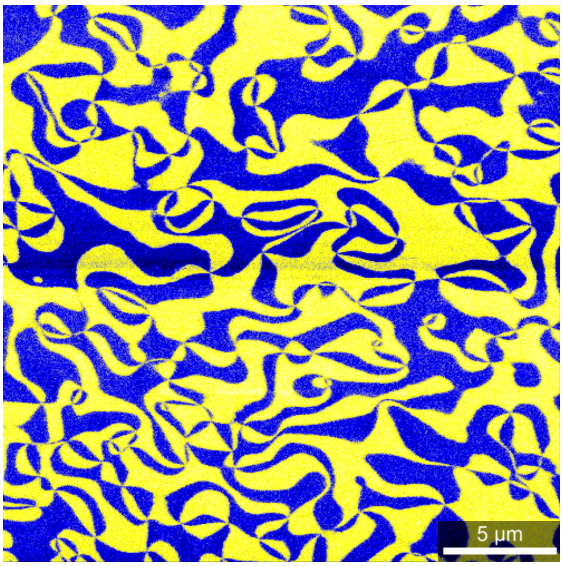

Fig. 2.6.: Domain structure of hexagonal manganite [34]. Blue and yellow areas show the two polarization states $+P$ and $-P$. Domains either meet at domain walls that are meandering through the sample or in vortex cores where six domains meet.

2.2.2. Mechanical stress

In 2013 Artyukhin et al. [31], proposed that considering a strain

$$f_{\text{strain}} = -GQ^2[(u_{xx} - u_{yy})\partial_x\Phi - 2u_{xy}\partial_y\Phi] \tag{2.18}$$

leads to an additional stable configuration of domains that does not include vortices. Instead a parallel array of domain walls, each with an increment of $\Delta\Phi = \pm\pi/3$ is the favored configuration. What they call a Φ-staircase can also be seen as stripe-like domains as each step of $\pi/3$ also implies a flip of the polarization direction. This was experimentally confirmed in 2014 by Wang et al. [35], where they applied mechanical strain in the in-plane direction on samples of different geometries and observed both areas with stripe-like domains in areas with high strain and vortex-like domains in areas of low strain. In their work they also confirmed that all vortex cores follow the same domain sequence ($\alpha-$, $\beta+$, $\gamma-$, $\alpha+$, $\beta-$, $\gamma+$) in clockwise direction, while all anti-vortex cores follow this same sequence in counter-clockwise direction. By comparing the transition region between vortex-like and stripe-like domains they could confirm that also the stripe-like domains follow this chirality.

Phase-field simulation

Xue et al. [36] solved the equation of the free energy density in rare-earth manganites numerically to further research the effect of strain on the domain structure. In Fig. 2.7 their results are shown where in the top half of the simulation box a strain was implied that increases from (a) to (d). In the initial state (a) with no strain, the system displays vortex-like domains in an isotropic fashion. As strain is applied in the top half, the domains there start to elongate towards the upper end of the box, some vortex cores are annihilated either on reaching the end of the system or by meeting an anti-vortex with opposite chirality. As the strain increases, the domains become more and more stripe-like until they reach a state of perfectly parallel domain walls. The number of vortex cores increases again as the stripes become narrower and therefore more in number. The strain-free bottom half of the simulation box stays isotropic with vortex-like domains. The domain structure is unaffected by the change in structure in the top half except for a small transition region between the two halves.

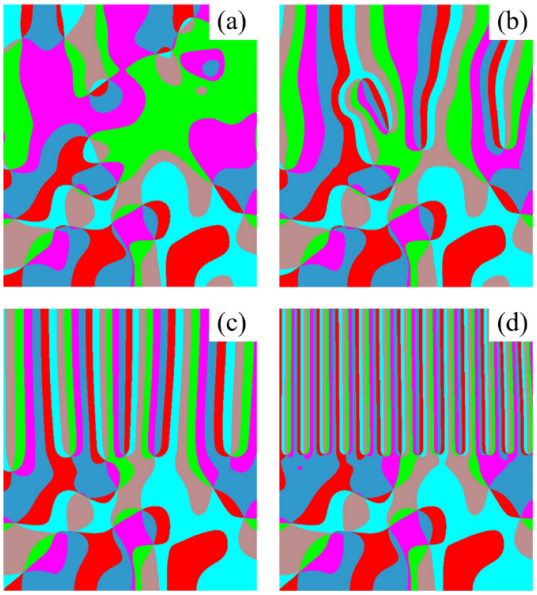

Fig. 2.7.: Phase field simulation of the effect of strain on the domain structure. From (a) to (d) an increasing strain is applied to the top half of the simulation box changing the domain structure from vortex-like to stripe-like in this region. [36]

2.3. Scaling behavior and Kibble-Zurek mechanism

In their works on topological defects, Tom Kibble and Wojciech Zurek developed a theory that describes the formation of domains and topological defects as a system undergoes a second order phase transition. The density of topological defects in their description depends on the rate at which the system is cooling down over the critical temperature. Their description has been applied to a broad range of systems, from astrophysical phenomena during the early stages of the universe [13–15] to superfluid helium [16, 17] all the way to colloidal systems [18] and even to ferroelectric crystals [10].
To determine over which distances microscopic states (such as polarization, magnetization, spin, etc.) influence each other inside a sample, an equilibrium correlation length ξ can be defined. The temperature dependence of the equilibrium correlation length was derived utilizing molecular field theories, as

$$\xi \propto |T - T_{crit}|^{-\nu} \tag{2.19}$$

where ν is again the critical exponent and T_{crit} the critical temperature. For ferroelectric systems, the critical temperature is referred to as Curie temperature. Eq. (2.19) can also

be written as

$$\xi(\epsilon) = \xi_0 |\epsilon|^{-\nu} \tag{2.20}$$

with the reduced distance parameter

$$\epsilon = \frac{T_{crit} - T}{T_{crit}} \tag{2.21}$$

Analogously an equilibrium relaxation time τ can be defined as

$$\tau(\epsilon) = \tau_0 |\epsilon|^{-z\nu}, \tag{2.22}$$

describing the time the system requires to reach its equilibrium state after being disturbed. The exponent z is called the dynamic critical exponent and it relates the spatial and temporal critical fluctuations. The material specific constants ξ_0 and τ_0 describe the correlation length and equilibrium relaxation time at zero temperature and can be determined using DFT calculations and experimental values. For $ErMnO_3$, Q.N.Meier et al. [10] show that $\xi_0 = 1.41\,\text{Å}$. It is important to note that both ξ and τ diverge at the so called critical point where $T = T_{crit}$ as shown in Fig. 2.8 by the blue lines.

In their theory, Kibble and Zurek [13–17] assume that a sample is cooled down linearly through T_{crit}, that means that the temperature parameter ϵ changes linearly with time t and can therefore be expressed as

$$\epsilon = \frac{T_{crit} - T}{T_{crit}} \tag{2.23}$$

$$= \frac{t}{\tau_Q} \tag{2.24}$$

where τ_Q is the characteristic time set by the cooling rate.
Far away from the critical temperature, so for $|\epsilon(t)| >> 0$, the equilibrium relaxation time is very small compared to the time it takes for the system to reach its critical point. That means that the order parameter always has time to reach its equilibrium state. The process is essentially adiabatic. As $|\epsilon(t)|$ gets close to zero, $\tau(\epsilon)$ diverges according to eq. (2.22), implying that the the system has no time to reach its equilibrium state before

the critical point is reached. Therefore the dynamics in the system can effectively be seen as frozen.

From this argument, Zurek suggests [17] to separate the phase transition into three separate zones, so that the system goes from adiabatic to frozen and to adiabatic again. This idea is sketched in Fig. 2.8 where the correlation time is plotted over the time difference $t - t_{crit}$. The white areas to the left and right denote the adiabatic regimes and the blue in the center shows the frozen-out regime.

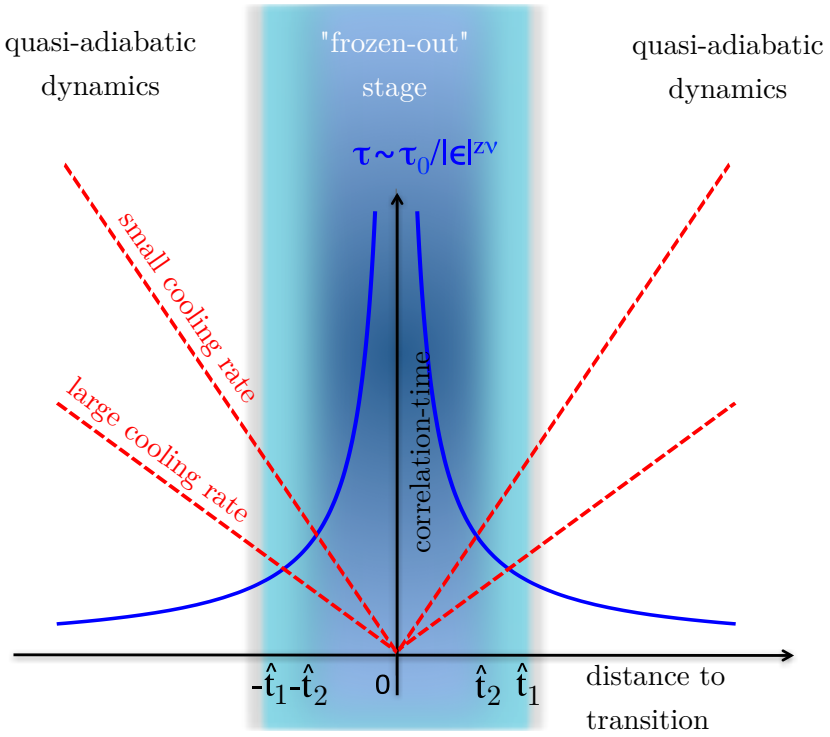

Fig. 2.8.: Cooling of a sample showing a second order phase transition. On the x-axis the time difference $t_{crit} - t$, on the y-axis the correlation time. τ (blue) diverges exponentially at $t_{crit} - t = 0$ while the $|\frac{\epsilon}{\dot{\epsilon}}| = t$ (red) has a linear slope. The process can be split into three regimes: Two adiabatic regimes far away from the critical point where the order parameter can always reach its equilibrium state and a frozen regime in the middle. Here the order parameter will not reach equilibrium, because the relaxation time τ diverges. The freeze-out time $\hat{t}$, at which the regimes meet is used to predict the resulting domain size [37]. The meeting point where $t = \tau$ is changing with cooling rate and therefore $\hat{t}$ also depends on the cooling rate.

The dashed red lines represent the time at two different linear cooling rates, where the lower cooling rate results in a steeper slope than the higher cooling rate. The blue line shows the diverging relaxation time τ. The freeze-out time $\hat{t}$ is the point where the

cooling rate and the relaxation time are equal, so where their lines cross. This is the case when

$$\tau(t) \approx \left|\frac{\epsilon}{\dot{\epsilon}}\right| = t \tag{2.25}$$

with $\dot{\epsilon} = \partial\epsilon/\partial t$. $\hat{t}$ can therefore be found as

$$\begin{aligned}
\hat{t} &= \tau(\hat{t}) && (2.26)\\
&= \frac{\tau_0}{|\epsilon(\hat{t})|^{z\nu}} && (2.27)\\
&= \frac{\tau_0}{(\hat{t}/\tau_Q)^{z\nu}} && (2.28)\\
\Rightarrow \hat{t}^{1+z\nu} &= \tau_0 \tau_Q^{z\nu} && (2.29)\\
\Rightarrow \hat{t} &= \left(\tau_0 \tau_Q^{z\nu}\right)^{\frac{1}{1+z\nu}} && (2.30)
\end{aligned}$$

This implies that the order parameter lags behind, i.e., the system is not in equilibrium, for values of $\epsilon \in [-\hat{\epsilon}, \hat{\epsilon}]$, where

$$\begin{aligned}
\hat{\epsilon} &= \frac{\hat{t}}{\tau_Q} && (2.31)\\
&= \left(\tau_0 \tau_Q^{z\nu}\right)^{\frac{1}{1+z\nu}} \tau_Q^{-1} && (2.32)\\
&= \left(\frac{\tau_0}{\tau_Q}\right)^{\frac{1}{1+z\nu}} && (2.33)
\end{aligned}$$

A domain, as introduced is section 2.1.3, is defined as an area in which the microscopic states are all equal, for example in a ferroelectric the polarization vector points in the same direction. It is therefore practical to use the correlation length as a predictive tool for the domain size, because it gives a measure of the range over which the states influence each other. The average domain size can therefore be estimated by calculating the correlation length

$$\hat{\xi} = \xi(\hat{\epsilon}) \tag{2.34}$$
$$= \xi_0 |\hat{\epsilon}|^{-\nu} \tag{2.35}$$
$$= \left(\frac{\tau_Q}{\tau_0}\right)^{\frac{\nu}{1+z\nu}} \tag{2.36}$$

$\hat{\xi}$ can then be used to find the density of topological defects n in the system as

$$n \sim \frac{\hat{\xi}^d}{\hat{\xi}^D} \tag{2.37}$$
$$= \frac{1}{\xi_0^{D-d}} \left(\frac{\tau_0}{\tau_Q}\right)^{(D-d)\frac{\nu}{1+z\nu}} \tag{2.38}$$

where D and d denote the dimensions of the system and of the expected defects respectively. In a 3D system with 1D vortex cores as are found in $ErMnO_3$, that means that $D - d = 2$ and therefore that

$$n \sim \frac{1}{\xi_0^2} \left(\frac{\tau_0}{\tau_Q}\right)^{\frac{2\nu}{1+z\nu}} \tag{2.39}$$

Eq. (2.39) is known as „Kibble-Zurek“ equation and gives a direct relation between the cooling rate over T_{crit} that a sample undergoes and the resulting density of topological defects.

2.4. Piezoresponse force microscopy

In order to visualize the domain structure in a ferroelectric material, the fact that every ferroelectric material is also piezoelectric is very useful. Piezoresponse force microscopy (PFM) is a technique that can measure the piezoelectric properties on the nanoscale. Due to the different orientation of the ferroelectric domains and the resulting different piezoelectric response, this technique gives information on the domain structure of ferroelectric materials.

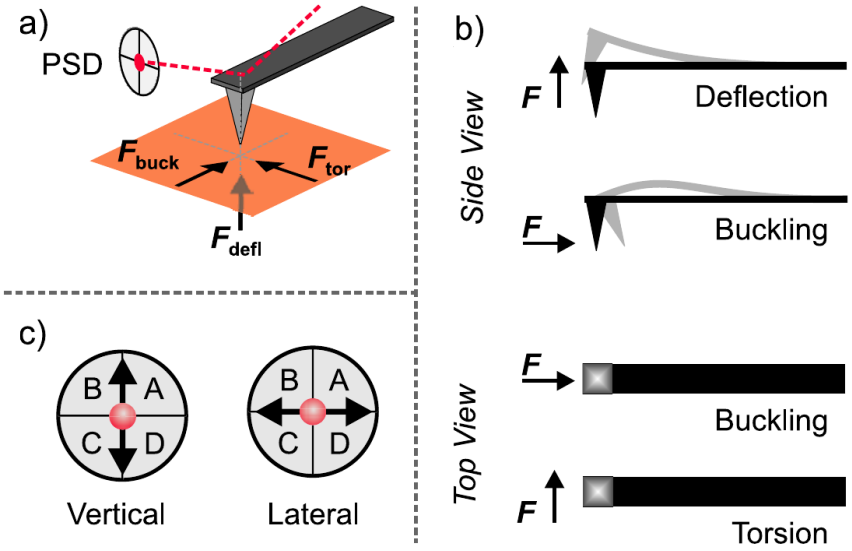

Fig. 2.9.: Setup of a piezoresponse force microscope [38]. (a) shows the cantilever, where a laser light is reflected onto a photodetector. The arrows show the direction in which the sample can expand and contract and the corresponding reaction of the cantilever (buckling, torsion, deflection). (b) shows a sketch of the cantilever and its different types of distortion from side and top view. (c) shows the photodetector that is split into four sections. Each type of distortion leads to the laser beam being moved in a different direction and thus hitting a different quadrant of the photodetector. The signal is split into vertical and lateral that is read out separately.

Fig. 2.9 shows the working principle of a PFM setup. A cantilever that has a conductive tip of few nanometers in diameter, is in contact with the sample. A laser beam is shone on the top surface of the cantilever in such a way that is reflected onto a photodetector as shown in Fig. 2.9 (a). The detector is separated into four quadrants as shown in Fig. 2.9 (c) and initially the laser hits the central spot between the four parts. Then an AC voltage is applied between the cantilever and the backside of the sample, causing the sample to expand and contract because of its piezoelectric properties. Different polarization states cause the sample to expand in a different direction. This causes the cantilever to be distorted as shown in Fig. 2.9 (b), which in turn is monitored by the laser position on the detector. There are different types of deformation the cantilever can undergo i.e. buckling, deflection and torsion, which each have a different effect on the laser displacement. Which type of distortion is happening is determined by the direction in which the material is moving. It is not only the type of distortion that is measured, but also the phase. As an AC current is applied, the material will expand and contract with the same frequency, but $+P$ and $-P$ domains will show a phase shift

of π in their oscillation, because they show an opposite reaction the the applied field. With this method the different domains can be made visible [38–40]. To determine the exact polarization states of the domains, more advanced methods like vector PFM are necessary.

3. Experiment

3.1. Sample preparation

High-purity $ErMnO_3$ powder is manufactured using solid-state synthesis using Er_2O_3 (99.9 % Purity; Alfa Aesar, Haverhill, MA, USA) and Mn_2O_3 (99.0 % Purity; Sigma-Aldrich, St. Louis, MO, USA). More details can be found in ref. [12]. 0.5 g of this powder is pressed into flat cylindrical pallets with a diameter of 1 cm for each sample. To ensure isotropic pressure distribution on the sample a coldisostatic press is used (Autoclave Engineers, Parker-Hannifin, Cleveland, OH, USA) to exert a pressure of 29 000 psi (≈200 MPa).

3.2. Furnace calibration

Before sintering the sample, one needs to ensure that the thermo-element inside the furnace is accurate enough. Therefore the furnace is heated to T_C. Fig. 3.1 shows the temperature profile of an external thermocouple that is inserted into the tube of the furnace. The tube itself has a length of 120 cm, the thermocouple is inserted to half the length, because the temperature profile is assumed to be symmetric. The insertion depth is measured from the end of the tube. The tube sticks outside the box of the furnace, in which the heating elements are sitting. That means that for small insertion depths the temperature is far too low, because the thermocouple, while already in the furnace tube, is still outside the heated box of the furnace. As the thermocouple approaches the center of the furnace, the temperature gets closer and closer to the target value. The 6 cm to each side of the middle have exactly the target temperature.

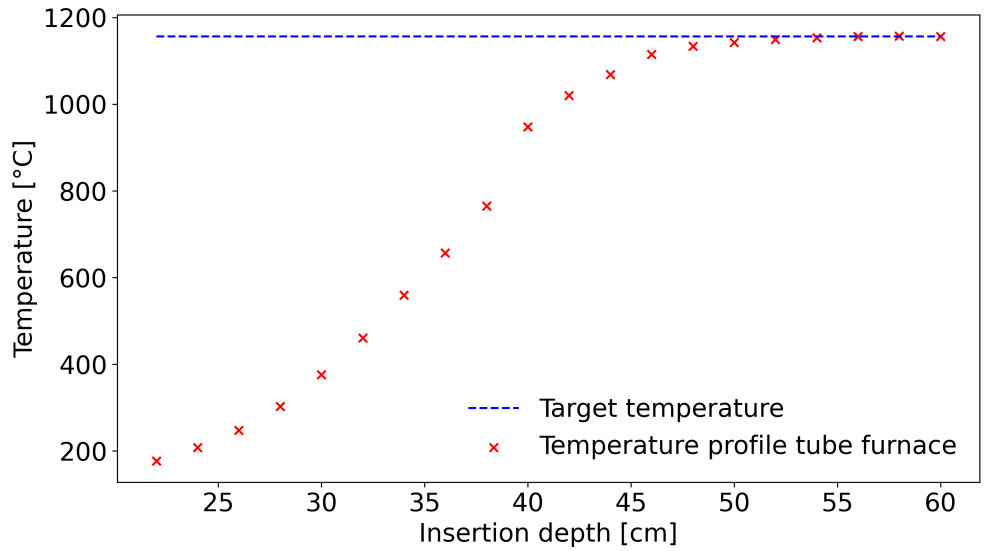

Fig. 3.1.: Temperature profile inside the tube furnace. The insertion depth measures, how far the thermocouple is inserted into the tube of the furnace. In the center of the furnace (at 60 cm depth) and up to 6 cm to the side of it, the set temperature is exactly on point with the measured temperature. This way it is ensured that T_C is inside the 40 K cooling range.

3.3. Cooling rate experiment

For sintering the sample, it is heated to a temperature above the T_C as illustrated in Fig. 3.2. For this experiment a sintering temperature $T_s = 1475\,°C$ was chosen, with a dwell time of 24 h. Those conditions were chosen to achieve grains large enough to host multiple domains as explored in ref. [12]. To ensure that the grain size is equal for all samples the dwell time at T_s was chosen to be long, to minimize the driving forces for grain growth during the cooling process [12].

Cooling down after the sintering process the actual experiment is conducted: Each sample is cooled through T_C at a different cooling rate. For all samples a cooling rate of 5 K/min is chosen, except for a 40 K interval around T_C. From 1176 °C to 1136 °C the cooling rate is adjusted to the different values needed for the experiment. The cooling rates chosen are 10^{-2} K/min (blue), 10^{-1} K/min (green), 10^{0} K/min (yellow) and 10^{1} K/min (red). This procedure is similar to the work done on single crystals by Q.N. Meier et al. [10].

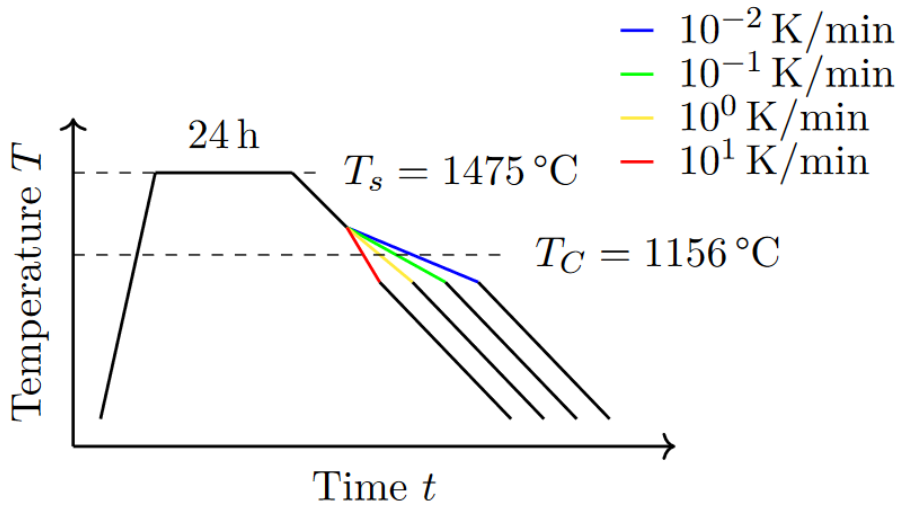

Fig. 3.2.: Temperature profile for sintering the samples. The tube furnace is heated to the sintering temperature $T_s = 1475\,°C$ and left to dwell there for 24 h. Afterwards it is cooled to 1176 °C with a rate of 5 K/min. From 1176 °C to 1136 °C the cooling rate is set to four different values of 10^{-2} K/min (blue), 10^{-1} K/min (green), 10^{0} K/min (yellow) and 10^{1} K/min (blue). Having crossed T_C with the respective rate, the cooling to room temperature continues at 5 K/min.

3.4. Piezoresponse force microscopy

After the sintering and cooling the samples are lapped with 9 µm calcinated aluminum oxide solution (Logitech, Glasgow, UK) in order to image the bulk of the sample. The chemical composition and the mechanical boundary conditions might be different at the sample surface. Furthermore the surface is exposed to air, which might lead to unwanted reactions. To also get rid of topographic influences and to make atomic force microscopy (AFM) measurement possible, the sample is polished to a root mean square (RSM) of ca. 20 nm (averaged over 1500 µm^2 per sample) after lapping, using a mechano-chemical procedure with an SF1 polishing suspension (Logitech, Glasgow, UK).
That the lapping and polishing is only possible in this fashion, because the hexagonal manganites are not ferroelastic, so the mechanical force applied has no impact on the domain structure.
The PFM images were obtained using a NT-MDT Ntegra Prisma setup (NT-MDT, Moscow, Russia) measuring off-resonance at a frequency of 40.13 kHz with an amplitude of 10 V. The tip used was platinum coated Spark 150 pt (NuNano, Bristol, UK). To

enhance the weak signal from the off-resonance two lock-in amplifiers were used (SR830, Stanford Research Systems, Sunnyvale, CA, USA).

3.5. Image analysis

3.5.1. Grain size and Vortex density

The grain size is determined using the image program imageJ. To determine the number of pixels of one grain P_{grain}, a polygonal shape is drawn along the grain boundaries, for which the program then gives a pixel count. To calculate the real grain size A_{grain}, P_{grain} is divided by the total number of pixels in the whole image P_{image} and multiplied by the area of the image A_{image}.

$$A_{grain} = \frac{P_{grain}}{P_{image}} \cdot A_{image}. \tag{3.1}$$

The number of vortex cores n in each grain is counted manually and the vortex density ρ is calculated as

$$\rho = \frac{n}{A_{grain}}. \tag{3.2}$$

To make understanding more intuitive, the grains are then assumed to be approximately circular so that the grain radius r can be calculated as

$$r = \sqrt{\frac{A_{grain}}{\pi}}. \tag{3.3}$$

3.5.2. Stripe periodicity

To calculate the average domain frequency for a sample, 20 profiles are drawn through periodic domain structures as demonstrated in Fig. 3.3a. The profiles show the pixel values for each pixel contained in the drawn lines. To correct for noise, the line is chosen to be 30 pixels wide, which are averaged together to give one value in the profile, which is plotted in Fig. 3.3b. Applying a fast fourier transform then gives the frequency of each profile. Of the resulting spectrum, only the highest peak was considered as shown in Fig. 3.3d. The peak in the frequency spectrum at $0\,\mu m^{-1}$ is ignored for this method as it is caused by uncorrelated features in the profile. To confirm the function of this method, the domain frequency was additionally calculated manually for individual samples by counting the domains and dividing by the length of the profile as demonstrated in Fig. 3.3c. The frequency values for all 20 profiles are then averaged to give one mean

value per image and the standard deviation is used as error. The individual values are used to create a distribution of frequencies, which again contains further information on how the domain structure changes from sample to sample.

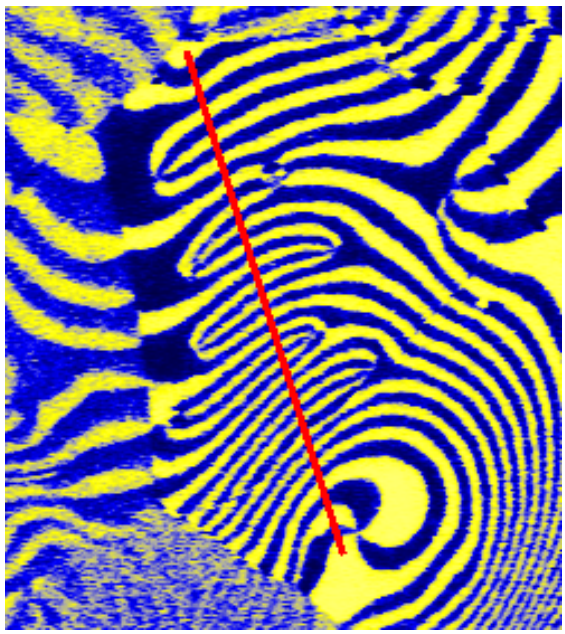

a)

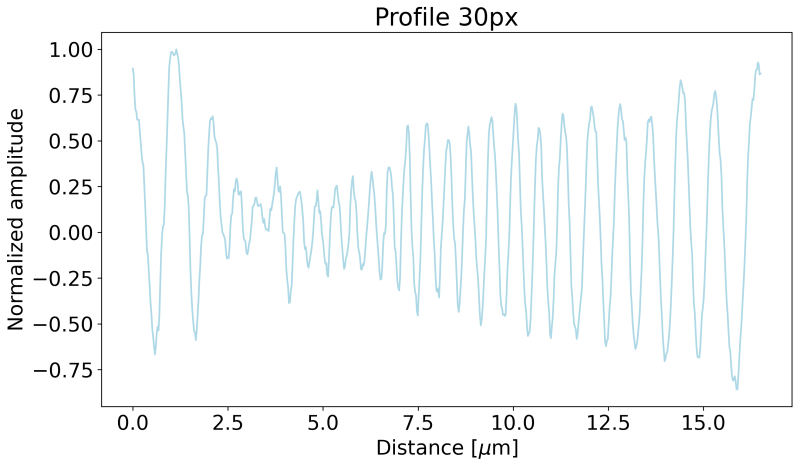

b)

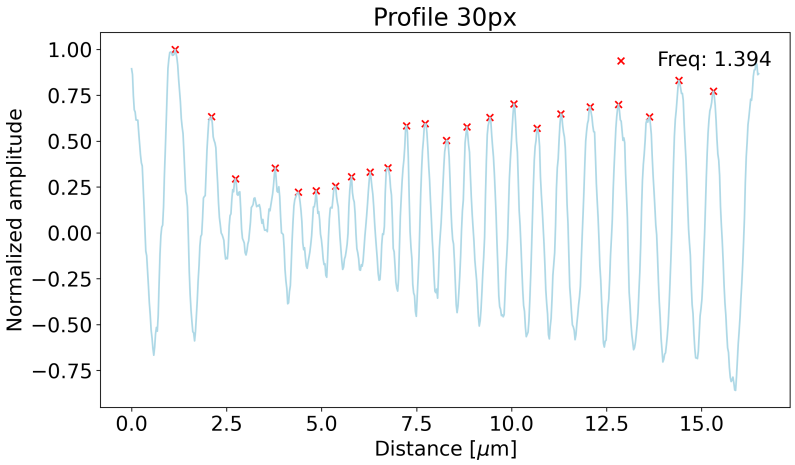

c)

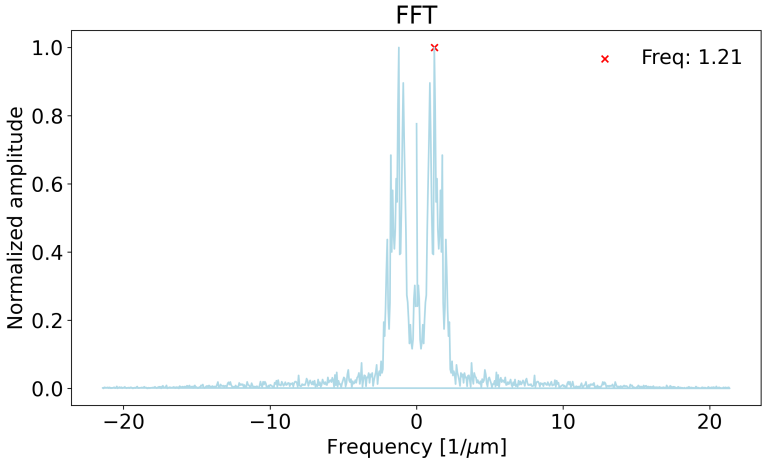

d)

Fig. 3.3.: Image analysis method to measure the domain frequency of stripe-like domains. a), b) The profile of a periodic feature is extracted. c) The number of peaks divided by the length of the profile gives an estimate of the frequency. d) Fourier transform gives a precise measure of the frequency.

4. Results

4.1. Microstructural analysis

Fig. 4.1 shows a topography scan of the sample surface of the polycrystalline $ErMnO_3$ taken with the AFM. It is corrected by a 6th-order polynomial so that any tilt or bend of the surface is removed and only features that can not be accounted for by an uneven surface are visible. Several features can be noted: The dark spots that are visible are pores in the sample, the biggest of which is located in the top left corner of the scan. They can be so deep that the AFM tip can not follow them to get a signal and are therefore completely dark. For the same reason they will not give PFM contrast and will equally appear as dark spots in the PFM scans shown in Fig. 4.3.
Secondly there are dark outlines visible that crate a web throughout the sample. Some of them correspond to grain boundaries as shown in the blue inset. Others are microcracks that appear after domain formation when cooling down the sample, as is known to happen for polycrystalline ceramics [41–43]. To tell one from the other is not possible using only topography, but electron backscattered diffractometry (EBSD) or analysis of the domain structure using PFM can help in the matter.
The small, slightly darker spots that appear on many of the grains are dirt particles that are sitting on the sample surface. These features are found in all samples equally (see more images in appendix A).

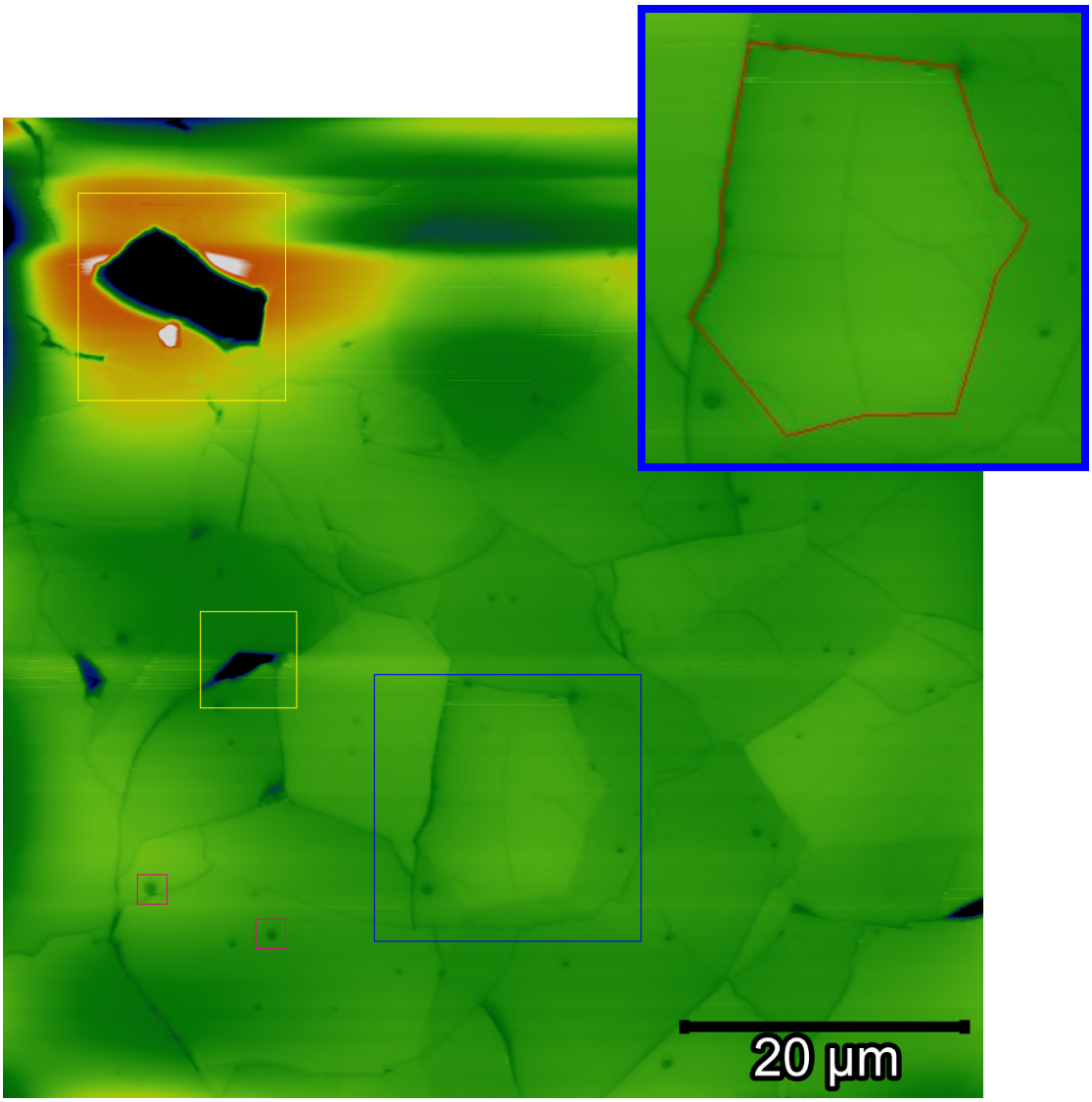

Fig. 4.1.: Topographic image of polycrystalline $ErMnO_3$ revealing grain boundaries, microcracks, pores and dirt particles on the sample surface. The blue inset shows an example grain boundary in red, while the dark lines inside the marked grain are microcracks. The pink boxes show examples of dirt particles on the sample, the yellow boxes frame examples of pores.

4.2. Grain size

To investigate the grain size, an average of 20 grains on each PFM image shown in Fig. 4.3 were analyzed by using imageJ as described in section 3.5. The quantitative analysis of the grain size in Fig. 4.2 shows that the grains have an average radius between

16.5 µm (10^{-2} K/min) and 10.9 µm (10^{1} K/min), so they differ by about a factor of 2. The trend seen in Fig. 4.2 is that with increasing cooling rate, the grain size decreases. The error bars are given by the standard deviation. The change in domain structure in this experiment is therefore solely caused by the change in cooling rate and not influenced by a change in grain size.

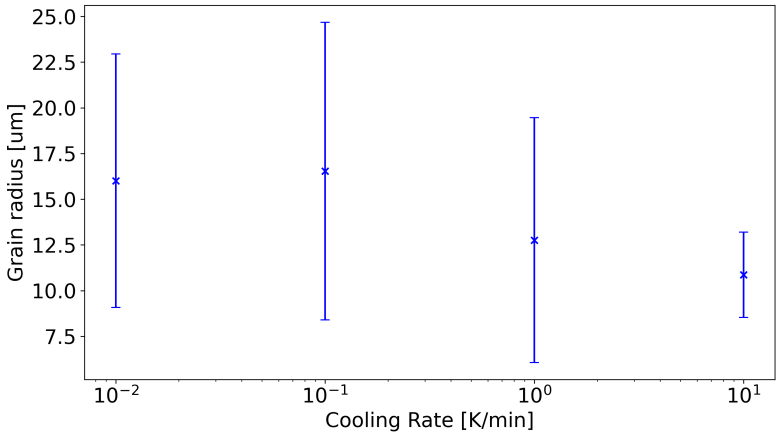

Fig. 4.2.: Grain size as a function of the cooling rate in the different samples. The grains that were cooled more slowly show slightly bigger grains than the ones cooled with a high cooling rate.

4.3. Nanoscale electromechanical analysis

Fig. 4.3 shows the piezoresponse of the four samples cooled at different rates as described in section 3.3. Subfig. a)-c) show the out-of-plane signal, while subfig. d) shows the in-plane signal), the respective other image can be found in Appendix B. The yellow and blue colors indicate areas of opposite response signal. This signal is directly related to the polarization state of the material and therefore shows the underlying ferroelectric domain structure. In all four samples similar patterns are revealed: In the center of the individual grains, vortex cores can be found while towards the grain boundaries stripe-like domains are the predominant form. All vortex cores exhibit the six-fold symmetry that was discussed in section 2.2.1. In some smaller grains there are no vortex cores present at all. In most cases, stripe-like domains meet the grain boundaries at a 90° angle. It can be noted that in places where the domains are in stripe-like formation, the domain walls are mostly parallel and the width of the domains is about the same for all stripes in that region. There is no preferential direction in the system, neither for the orientation of the stripes inside one grain, nor for the grain orientation in the sample.

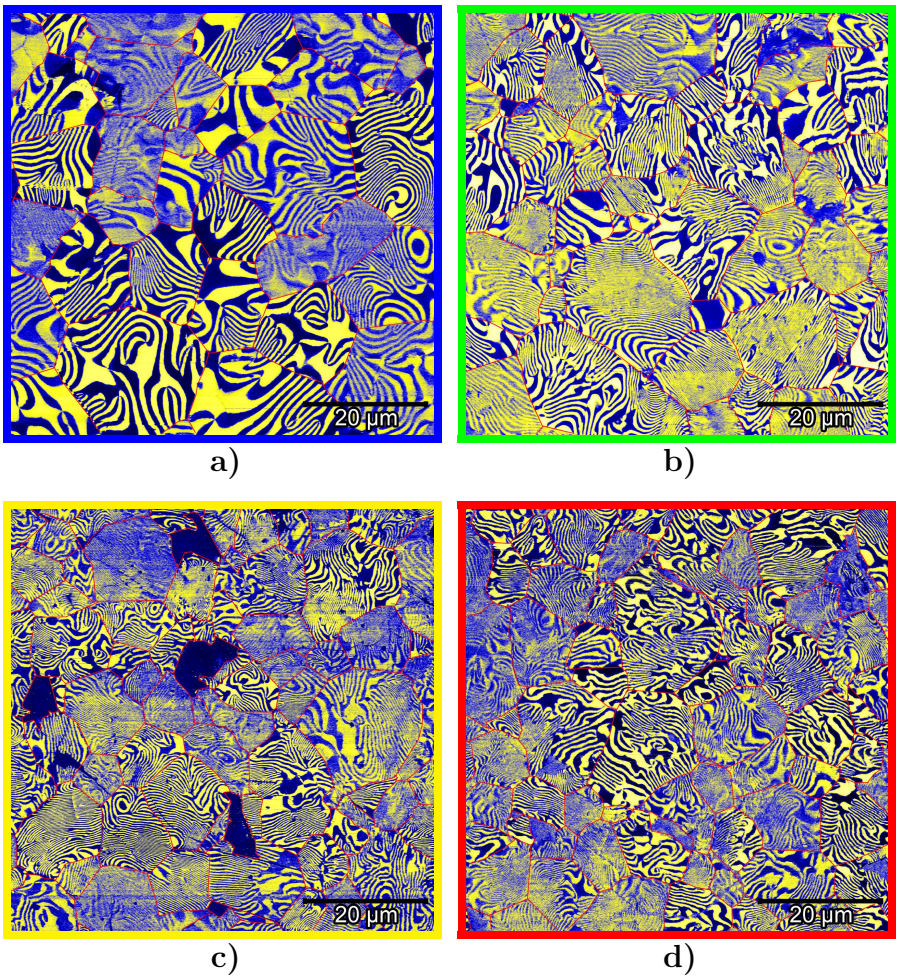

Fig. 4.3.: Domain structure of $ErMnO_3$ at different cooling rates over T_C: a) 10^{-2} K/min, b) 10^{-1} K/min, c) 10^{0} K/min, d) 10^{1} K/min. a)-c) show the normal contrast, while d) shows the lateral contrast. The grain boundaries have been outlined in red for better visibility. As the cooling rate increases, the domain size visibly decreases and the domain shape changes from isotropic and vortex-like to more stripe-like patterns.

Aside from the well known structure of the hexagonal manganites, an additional effect can be observed: As the cooling rate increases, the domains decrease in size. Where in Fig. 4.3a (10^{-2} K/min) a grain sometimes contains only about ten domains and a single vortex core, the grains in Fig. 4.3d (10^{1} K/min) often contain many more domains. The domain structure also seems to change. Even though both vortex-like and stripe-like domains are present in all samples, the distribution changes. In Fig. 4.3a (10^{-2} K/min), large areas are taken up by vortex-like domains while the stripe-like domains mostly

form close to the grain boundaries. In Fig. 4.3c (10^0 K/min) on the other hand there are only very few vortex-like domains. Often the whole grain is permeated by stripe-like domains. There are still many vortex cores to be seen, but only few domains end in more than one vortex core, most extend from one vortex core to the grain boundary.

4.4. Vortex density and domain frequency

4.4.1. Vortex density

Fig. 4.4 shows the vortex density in the samples of different cooling rates where the error bars show the standard deviation. To obtain these results, the grain sizes on the PFM scans for each sample were calculated as described in section 3.5. The number of vortex cores was counted manually for each grain and then divided by the total area of the grain (eq. (3.2)). For the analysis, the same grains were used as for the grain size analysis, so again an average of 20 grains per sample. For the cooling rates 10^{-2} K/min, 10^{-1} K/min and 10^0 K/min an increase in vortex density by ca. 200% can be seen, while the vortex density at 10^1 K/min is decreased again.

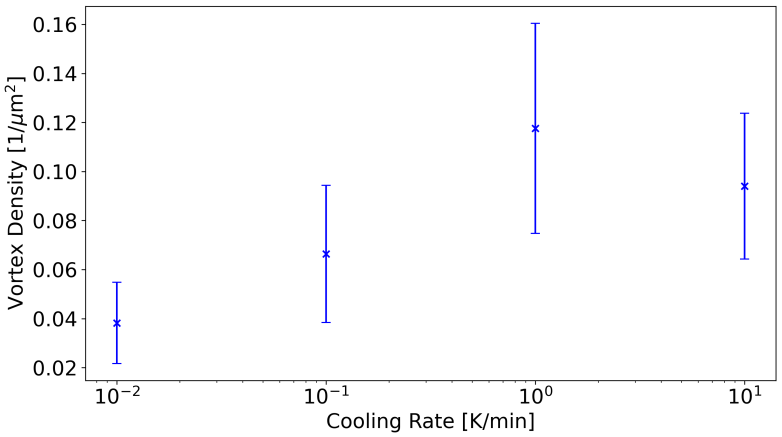

Fig. 4.4.: Vortex density at different cooling rates. The vortex density increases with increasing cooling rate on a logarithmic scale. For a cooling rate of 10^1 K/min, the average vortex density is reduced.

From the vortex density the correlation length $\hat{\xi}$ can be calculated by solving eq. (2.38) for $\hat{\xi}$ so that

$$n \sim \frac{\hat{\xi}^d}{\hat{\xi}^D} = \frac{1}{\hat{\xi}^2} \tag{4.1}$$

$$\Rightarrow \hat{\xi} \sim \frac{1}{\sqrt{n}} \tag{4.2}$$

The resulting values for the correlation length lie between 2.8 µm (10^0 K/min) and 5.0 µm (10^{-2} K/min).

4.4.2. Domain frequency

As the vortex density only gives a measure for the vortex-like domains, the stripe-like domains need to be investigated separately. The number and size of stripe-like and vortex-like domains are not necessarily directly correlated, as not every stripe-like domain ends in a vortex core. It can indeed in some grains be seen that stripe-like domains cross through the whole grain without meeting a vortex core, both ends terminating at a grain boundary. Therefore the spatial frequency of the stripe-like domains was determined as described in section 3.5.
Fig. 4.5 shows the spatial frequency of the stripe-like domains for the different samples. Qualitatively it shows the same trend as Fig. 4.4: For the cooling rates 10^{-2} K/min, 10^{-1} K/min and 10^{-0} K/min the domain frequency increases from 1.00 1/µm to 1.70 1/µm while the domain frequency at 10^1 K/min is lowered to 1.47 1/µm.

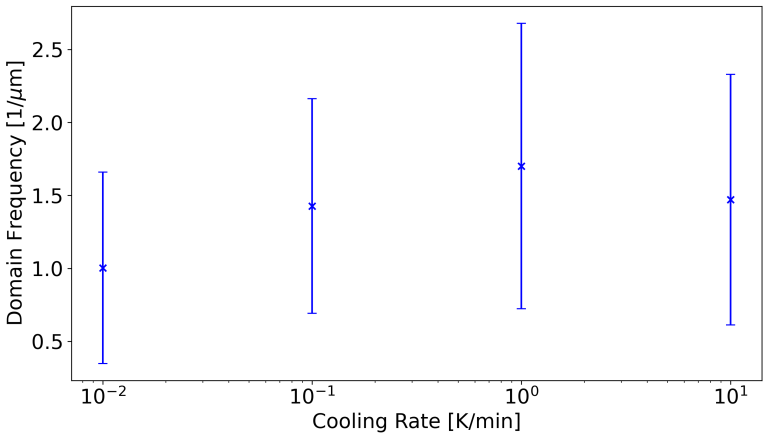

Fig. 4.5.: Domain frequency at different cooling rates. The domain frequency shows a trend similar to the vortex density in Fig. 4.4. It increases at first, followed by a drop at a cooling rate of 10^1 K/min.

To get more insight into how the stripe-like domain structure varies with cooling rate, the distributions of domain frequencies were plotted in Fig. 4.6. Each distribution contains 80 single values obtained as described in section 3.5. All four distributions roughly follow a Gaussian distribution, but it is apparent that the statistics of 80 values is not enough to give a smooth curve. With changing the cooling rate, two things change: the position of its maximum μ and its width given by the standard deviation σ. The positions of the maxima confirm the results of Fig. 4.5, but the width gives further information. In Fig. 4.6a the distribution is quite narrow ($\sigma = 0.355$), while for the others it becomes a lot wider, e.g. in Fig. 4.6c ($\sigma = 0.718$). This shows that not only the median value of the domain frequency changes, but also that the domain size in the sample cooled at 10^{-2} K/min is much more homogeneous than in samples that are cooled with a higher cooling rate. This can also be confirmed by the PFM images Fig. 4.3 where the visible domains are all roughly of the same size. In Fig. 4.3d on the other hand there are still some domains that are quite big while some stripe-like domains are so narrow that they are barely resolved.

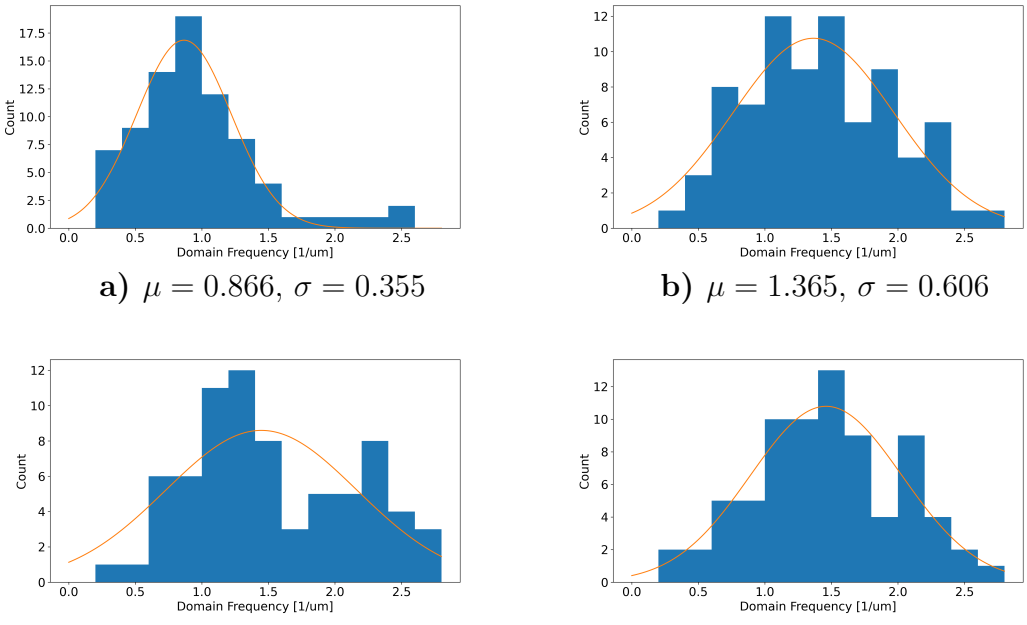

a) $\mu = 0.866$, $\sigma = 0.355$ **b)** $\mu = 1.365$, $\sigma = 0.606$

c) $\mu = 1.447$, $\sigma = 0.718$ **d)** $\mu = 1.46$, $\sigma = 0.57$

Fig. 4.6.: Distribution of domain frequencies for each cooling rate: a) 10^{-2} K/min, b) 10^{-1} K/min, c) 10^{0} K/min, d) 10^{1} K/min. They can be approximated by a Gaussian distribution, the position μ and standard deviation σ of which give further information on the domain structure.

5. Discussion

5.1. Microstructure

As described in section 4.1, all samples show the same general features of microcracks, dirt, pores and grain boundaries. No significant change in the number of pores and cracks can be seen, it is therefore safe to assume that the cooling rate does not impact those features in a major way, as was already discovered for other manganites [44]. The grain size on the other hand changes by about a factor of 2 as shown in Fig. 4.2. This effect is most likely not directly caused by the cooling rate itself, but by the fact that having a low cooling rate also means that the sample is at a higher temperature for a longer time. The grain growth happens mostly at $T_S = 1475\,°\mathrm{C}$, but it can also happen at lower temperatures. The sample that is cooled at $10^{-2}\,\mathrm{K/min}$ for example takes more than 70 h to cool down to room temperature, while it only takes 11 h for the sample cooled at $10^{-1}\,\mathrm{K/min}$. The effect of grain size on the domain structure has been studied by Schultheiß et al. in ref. [12], where they show that the domain size decreases with increasing grain size. At their proposed scaling rate of $d = g^{-0.1}$ a factor of 2 in grain size leads to a factor 0.933 in domain size, which is negligible for the purposes of this study.

5.2. Domain structure in polycrystals

The origin of ferroelectricity in the polycrystalline $ErMnO_3$ is the same as in single crystals, therefore the domain structure is also similar. The material is still uniaxial even though the orientation of the polarization direction can vary from grain to grain and the topological defects in form of vortex cores can still be seen throughout the sample. However the presence of stripe-like domains is a feature that occurs much less frequently in single crystals. Their existence can be attributed to intergranular strain fields appearing during the sintering process when the grains form and when their crystal structure changes upon cooling down, causing the grains to accumulate elastic strain. Because of their anisotropic expansion coefficient and different grain orientation, the expansion of each grain has a different direction, causing the grains to press against

each other. The resulting strain leads to other stable domain configurations where the domains run parallel to each other and that do not include vortex cores [12, 35] as discussed in section 2.2.2. The fact that even though the strain fields permeate multiple micrometers deep into the grains there are still large areas where vortex cores are present can be attributed to the fact that there are areas of zero strain fields in the center of the grain [45]. This also accounts for the inverse scaling behavior observed by Schultheiß et al. in [12], because as the grains get bigger, the overlap of opposite strain field is smaller. In this way they can effectively impose more of their effect on the sample, thus producing more stripe-like domains and resulting in a smaller domain size. Since the average domain size is approximately equal throughout the sample, this effect does not account for changes in the average domain size between the samples.

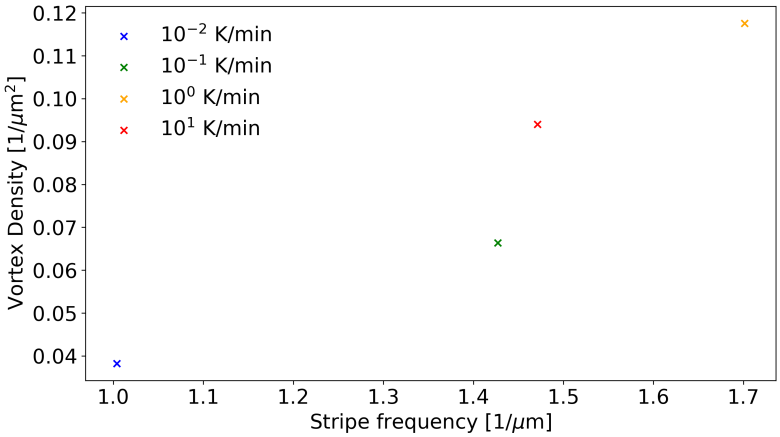

Fig. 5.1.: Vortex density plotted over the stripe frequency for the different cooling rates. The data points for cooling rates of 10^{-2} K/min to 10^{0} K/min show that the vortex density increases with stripe frequency, which matches the results from Fig. 4.5 and Fig. 4.4.

To analyze the connection between stripe-like and vortex-like domains more closely, the vortex density is plotted over the stripe frequency in Fig. 5.1. Note that this plot does not give a causality, but a correlation. Here a clear trend can be seen that as the stripe frequency increases, so does the vortex density. It can not be extracted if the scaling is linear, because too few data points are given. That the vortex density and the stripe frequency are dependent on each other is expected since most of the stripe-like domains end in a vortex core on one end and most vortex cores are connected to stripe-like domains. The only exceptions are stripe-like domains that run all the way through the grain without meeting a vortex core and areas where the domains are purely vortex-like.

5.3. Scaling behavior & Kibble-Zurek mechanism

To investigate the impact of polycrystallinity on the formation of topological defects, the vortex density that was measured for the polycrystalline samples is compared to literature values measured from single crystalline $ErMnO_3$ by Q.N. Meier et al. [10] as shown in Fig. 5.2. The blue polycrystalline data here show the same trend as the single crystal shown in red, i.e. the vortex density increases with cooling rate, but the effect is strongly suppressed. A fit with the Kibble-Zurek equation eq. (2.39) for both data sets yields that the Kibble-Zurek exponent $K = \frac{2\nu}{1+z\nu}$ is decreased from $K = 0.49$ for the single crystal to $K = 0.13$ for the polycrystal. The scaling exponent $K = 0.49$ is a universal constant for all hexagonal manganites in the single crystalline state as shown in ref. [10]. The two main effects that can be held responsible for this change in scaling behavior are the finite system size and the intergranular strain fields, which will individually be discussed in the following sections.

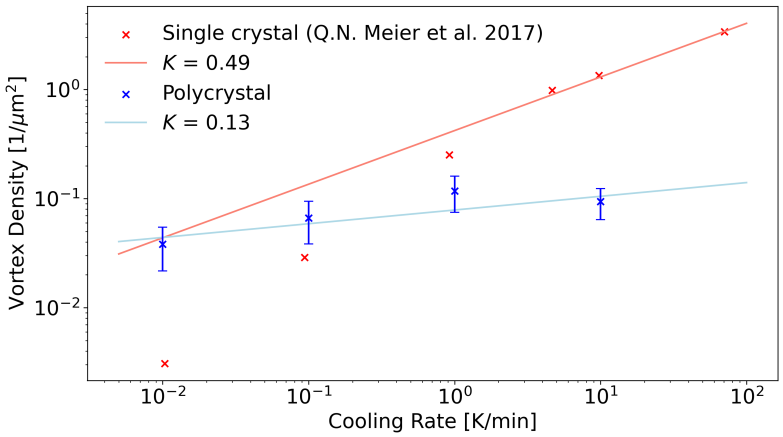

Fig. 5.2.: Vortex density as a function of cooling rate. The vortex density increases logarithmically with the cooling rate according to the Kibble-Zurek scaling. The Kibble-Zurek exponent determines the slope of the curve on a log-log scale and differs by a factor of 4 between the single crystal and the polycrystal.

5.3.1. Finite system size

A single crystal is in principle a perfect system: There is an approximately infinite number of atoms that have a perfectly periodic structure, each atom behaves exactly the same as it experiences the same potential as every other atom. Only very few atoms sit on the surface of a single crystal that could behave differently and those are usually not used in measurements for exactly that reason. In a polycrystalline material, things

are not quite as simple: The total surface area of the individual crystals is many times as large as that of a single crystal, the surface atoms are also part of the measurement, neighboring crystals can influence each other and the individual crystals can not be regarded as infinite anymore. In short: many edge effects start playing a role that can be disregarded in a single crystal.
For the formation of domains and vortex cores one aspect is particularly relevant: the correlation length. As discussed in section 2.3, the correlation length is the relevant quantity that determines the domain size after the phase transition from the paraelectric phase to the ferroelectric phase. What is not taken into account in the Kibble-Zurek mechanism is what happens when the system size is so small, that only few atoms do not experience the influence of the edge of the system, namely the grain boundary. This is the case for the samples used for this experiment where the correlation length is only a factor of 3-5 smaller than the grain size. In this case it might be energetically more favorable to have domains that terminate in a grain boundary rather than producing a vortex core. This would lead to a reduced number of vortex cores and a suppression of the Kibble-Zurek exponent as observed in Fig. 5.2.

5.3.2. Strain fields

As discussed in section 2.2.2, strain fields are responsible for the emergence of stripe-like domains in $ErMnO_3$. Those strain fields can either be applied mechanically [35] or can originate from intergranular tensions [12]. In their work, Xue et al. [36] demonstrate using phase-field simulations, that those strain fields can lead to the creation and annihilation as well as the movement of the vortex cores. The stronger the strain field becomes, the stronger also the influence on the vortex cores becomes [12, 35, 36]. More and more vortex cores are created to create stripe-like domains with a higher frequency, but at the same time more and more vortex cores are annihilated at the grain boundaries. It is therefore clear that strain fields play a role in the formation of vortex cores, but it is not clear if stronger strain fields lead to fewer or more vortex cores. One thing that was not investigated by Schultheiß et al. is the formation of stripe-like domains that are not connected to a vortex core. In Fig. 4.3 it can in some cases be seen, that domains cross a grain from one grain boundary to another without terminating in a vortex core. This is likely the effect of very strong strain fields in one direction that push out all the vortex cores in one area. This of course only works in a system where the individual grains are small enough that the strain fields permeate it strongly enough and where the vortex cores can annihilate at the grain boundary. Taking this effect into account it is reasonable to assume that strain fields alone do not necessarily change the vortex

density one way or another. In combination with a finite system however, out of which the vortex cores can be driven, they decrease the number of vortex cores in the sample and lead therefore to a suppression of the Kibble-Zurek exponent.

6. Conclusion

The goal of this work was to investigate the impact of polycrystallinity on the formation of topological defects following the Kibble-Zurek mechanism by means of a cooling rate study in polycrystalline $ErMnO_3$. For this study, four samples were prepared by solid-state synthesis that were then sintered at 1475 °C for 24 h to achieve constant grain size in the samples. Upon cooling down, the cooling rate over T_C was then adjusted to 10^{-2} K/min, 10^{-1} K/min, 10^{0} K/min and 10^{1} K/min respectively. The resulting domain structure was then visualized using PFM.

Analysis of the PFM images confirmed that the grain size throughout the samples is changing by less than a factor of 2, which is not significant enough to have an impact on the domain structure.

In the grains, two types of domains can be found: stripe-like and vortex-like domains. Both were analyzed separately by different methods. To get a measure of the stripe-like domains, their spatial frequency was determined, while the vortex-like domains were characterized by the vortex density. Both measures show the same qualitative trend, both stripe frequency and vortex density increase with increasing cooling rate up to a cooling rate of 10^{0} K/min and are then again reduced for 10^{1} K/min. A fit with the Kibble-Zurek function leads to the result that the Kibble-Zurek exponent for the polycrystal $K = 0.13$ is strongly suppressed in comparison to the single crystal where $K = 0.49$.

This different scaling is attributed to two different effects: On one hand, the finite system size that is limited by the grain boundaries. Grains that are on the same order of magnitude as the correlation length make the formation of vortex cores more unlikely, instead stripe-like domains are forming. On the other hand intergranular strain fields interact with the vortex cores. The strain fields also lead to a domain state that favors stripe-like domains and can lead to the vortex cores being pushed out of the grain.

To further research the interplay of strain and cooling rate during the formation of vortex cores, different combinations of strain and cooling rate should be applied and the parameter space should be explored in more detail.

Bibliography

[1] Joseph Valasek. "Minutes of the Washington Meeting, April 23 and 24, 1920". In: *Physical Review* 15 (1920), pp. 505–564. DOI: 10.1103/PhysRev.15.505.

[2] J. Valasek. "Piezo-Electric and Allied Phenomena in Rochelle Salt". In: *Physical Review* 17 (1921), pp. 475–481. DOI: 10.1103/PhysRev.17.475.

[3] Donghoon Kim et al. "Magnetoelectric Effect in Hydrogen Harvesting: Magnetic Field as a Trigger of Catalytic Reactions". In: *Advanced Materials* 34.19 (2022), p. 2110612. DOI: https://doi.org/10.1002/adma.202110612.

[4] J. A. Mundy et al. "Functional electronic inversion layers at ferroelectric domain walls". In: *Nature Materials* 16.6 (2017), pp. 622–627. DOI: 10.1038/nmat4878.

[5] Jakob Schaab et al. "Electrical half-wave rectification at ferroelectric domain walls". In: *Nature Nanotechnology* 13.11 (2018), pp. 1028–1034. DOI: 10.1038/s41565-018-0253-5.

[6] S. L. Miller et al. "Device modeling of ferroelectric capacitors". In: *Journal of Applied Physics* 68.12 (1990), pp. 6463–6471. DOI: 10.1063/1.346845.

[7] D. Damjanovic and R.E. Newnham. "Electrostrictive and Piezoelectric Materials for Actuator Applications". In: *Journal of Intelligent Material Systems and Structures* 3.2 (1992), pp. 190–208. DOI: 10.1177/1045389X9200300201.

[8] A. von Hippel. "Ferroelectricity, Domain Structure, and Phase Transitions of Barium Titanate". In: *Reviews of Modern Physics* 22 (1950), pp. 221–237. DOI: 10.1103/RevModPhys.22.221.

[9] Saidur R. Bakaul et al. "Freestanding Ferroelectric Bubble Domains". In: *Advanced Materials* 33.45 (2021), p. 2105432. DOI: https://doi.org/10.1002/adma.202105432.

[10] Q. N. Meier et al. "Global Formation of Topological Defects in the Multiferroic Hexagonal Manganites". In: *Physical Review X* 7 (2017), p. 041014. DOI: 10.1103/PhysRevX.7.041014.

[11] J. Schaab et al. “Imaging and characterization of conducting ferroelectric domain walls by photoemission electron microscopy”. In: *Applied Physics Letters* 104.23 (2014), p. 232904. DOI: 10.1063/1.4879260.

[12] Jan Schultheiß et al. “Confinement-driven inverse domain scaling in polycrystalline $ErMnO_3$”. In: *Advanced Materials* n/a.n/a (2022), p. 2203449. DOI: https://doi.org/10.1002/adma.202203449.

[13] T.W.B. Kibble. “Topology of cosmic domains and strings”. In: *Journal of Physics A: Mathematical and General* 9.8 (1976), pp. 1387–1398. DOI: 10.1088/0305-4470/9/8/029.

[14] T.W.B. Kibble. “Some implications of a cosmological phase transition”. In: *Physics Reports* 67.1 (1980), pp. 183–199. DOI: https://doi.org/10.1016/0370-1573(80)90091-5.

[15] T.W.B. Kibble and G. E. Volovik. “On phase ordering behind the propagating front of a second-order transition”. In: *Journal of Experimental and Theoretical Physics Letters* 65.1 (1997), pp. 102–107. DOI: 10.1134/1.567332.

[16] W.H. Zurek. “Cosmological experiments in superfluid helium?” In: *Nature* 317.6037 (1985), pp. 505–508. DOI: 10.1038/317505a0.

[17] W.H. Zurek. “Cosmological experiments in condensed matter systems”. In: *Physics Reports* 276.4 (1996), pp. 177–221. DOI: https://doi.org/10.1016/S0370-1573(96)00009-9.

[18] Sven Deutschländer et al. “Kibble-Zurek mechanism in colloidal monolayers”. In: *Proceedings of the National Academy of Sciences* 112.22 (2015), pp. 6925–6930. DOI: 10.1073/pnas.1500763112.

[19] Dragan Damjanovic. “Ferroelectric, dielectric and piezoelectric properties of ferroelectric thin films and ceramics”. In: *Reports on Progress in Physics* 61.9 (1998), pp. 1267–1324. DOI: 10.1088/0034-4885/61/9/002.

[20] Newnham Robert E. *Properties of Materials : Anisotropy, Symmetry, Structure.* OUP Oxford, 2005. ISBN: 9780198520757.

[21] L. Landau. “On the theory of phase transitions”. In: *Journal of Experimental and Theoretical Physics* 7 (1937), pp. 19–32.

[22] Wolfgang Nolting. *Phasenübergänge.* Berlin, Heidelberg: Springer Berlin Heidelberg, 2014, pp. 279–415. ISBN: 978-3-642-25393-5. DOI: 10.1007/978-3-642-25393-5_4.

[23] Martin Lilienblum. "Ferroelectric order in multiferroic hexagonal manganites". PhD thesis. ETH Zurich, 2016.

[24] B.A. Strukov and A.P. Levanyuk. *Ferroelectric Phenomena in Crystals: Physical Foundations*. Springer Berlin Heidelberg, 2012. ISBN: 9783642602931.

[25] R.A. Cowley. "Structural phase transitions I. Landau theory". In: *Advances in Physics* 29.1 (1980), pp. 1–110. DOI: 10.1080/00018738000101346.

[26] G. Arlt. "Twinning in ferroelectric and ferroelastic ceramics: stress relief". In: *Journal of Materials Science* 25.6 (1990), pp. 2655–2666. DOI: 10.1007/BF00584864.

[27] Dr. Irfan Lone et al. "Multiferroic ABO_3 Transition Metal Oxides: a Rare Interaction of Ferroelectricity and Magnetism". In: *Nanoscale Research Letters* 14 (2019). DOI: 10.1186/s11671-019-2961-7.

[28] W Prellier, M P Singh, and P Murugavel. "The single-phase multiferroic oxides: from bulk to thin film". In: *Journal of Physics: Condensed Matter* 17.30 (2005), R803–R832. DOI: 10.1088/0953-8984/17/30/r01.

[29] Bas B. Van Aken et al. "The origin of ferroelectricity in magnetoelectric $YMnO_3$". In: *Nature Materials* 3.3 (2004), pp. 164–170. DOI: 10.1038/nmat1080.

[30] Sinéad M Griffin and Nicola A Spaldin. "On the relationship between topological and geometric defects". In: *Journal of Physics: Condensed Matter* 29.34 (2017), p. 343001. DOI: 10.1088/1361-648x/aa7b5c.

[31] Sergey Artyukhin et al. "Landau theory of topological defects in multiferroic hexagonal manganites". In: *Nature Materials* 13.1 (2014), pp. 42–49. DOI: 10.1038/nmat3786.

[32] Craig Fennie and Karin Rabe. "Ferroelectric transition in $YMnO_3$ from first principles". In: *Physical Review B* 72 (2005). DOI: 10.1103/PhysRevB.72.100103.

[33] Michel A. Kervaire and John W. Milnor. "Groups of Homotopy Spheres: I". In: *Annals of Mathematics* 77.3 (1963), pp. 504–537.

[34] Lukas Puntigam et al. "Insulating improper ferroelectric domain walls as robust barrier layer capacitors". In: *Journal of Applied Physics* 129.7 (2021), p. 074101. DOI: 10.1063/5.0038300.

[35] X. Wang et al. "Unfolding of Vortices into Topological Stripes in a Multiferroic Material". In: *Physical Review Letters* 112 (2014), p. 247601. DOI: 10.1103/PhysRevLett.112.247601.

[36] Fei Xue et al. "Strain-induced incommensurate phases in hexagonal manganites". In: *Physical Review B* 96 (2017), p. 104109. DOI: 10.1103/PhysRevB.96.104109.

[37] Adolfo del Campo and Wojciech H. Zurek. “Universality of phase transition dynamics: Topological defects from symmetry breaking”. In: *International Journal of Modern Physics A* 29.08 (2014), p. 1430018. DOI: 10.1142/S0217751X1430018X.

[38] Elisabeth Soergel. “Piezoresponse force microscopy (PFM)”. In: *Journal of Physics D: Applied Physics* 44.46 (2011), p. 464003. DOI: 10.1088/0022-3727/44/46/464003.

[39] A. Gruverman and S. V. Kalinin. “Piezoresponse force microscopy and recent advances in nanoscale studies of ferroelectrics”. In: *Journal of Materials Science* 41.1 (2006), pp. 107–116. DOI: 10.1007/s10853-005-5946-0.

[40] Alexei Gruverman, Marin Alexe, and Dennis Meier. “Piezoresponse force microscopy and nanoferroic phenomena”. In: *Nature Communications* 10.1 (2019), p. 1661. DOI: 10.1038/s41467-019-09650-8.

[41] S. Galal Yousef et al. “Microcrack Evolution in Alumina Ceramics: Experiment and Simulation”. In: *Journal of the American Ceramic Society* 88.10 (2005), pp. 2809–2816. DOI: https://doi.org/10.1111/j.1551-2916.2005.00312.x.

[42] Monika Tomczyk et al. “Origin of microcracking in $YMnO_3$ ceramics”. In: *Scripta Materialia* 66.5 (2012), pp. 288–291. DOI: https://doi.org/10.1016/j.scriptamat.2011.11.014.

[43] M. Tomczyk et al. “Reduction of microcracking in $YMnO_3$ ceramics by Ti substitution”. In: *Scripta Materialia* 67.5 (2012), pp. 427–430. DOI: https://doi.org/10.1016/j.scriptamat.2012.04.042.

[44] Bo Fu et al. “Synthesis and properties of strontium-doped yttrium manganite”. In: *Journal of Materials Research* 9.10 (1994), pp. 2645–2653. DOI: 10.1557/JMR.1994.2645.

[45] Jan Schultheiß et al. “Quantitative mapping of nanotwin variants in the bulk”. In: *Scripta Materialia* 199 (2021), p. 113878. DOI: https://doi.org/10.1016/j.scriptamat.2021.113878.

A. Topography

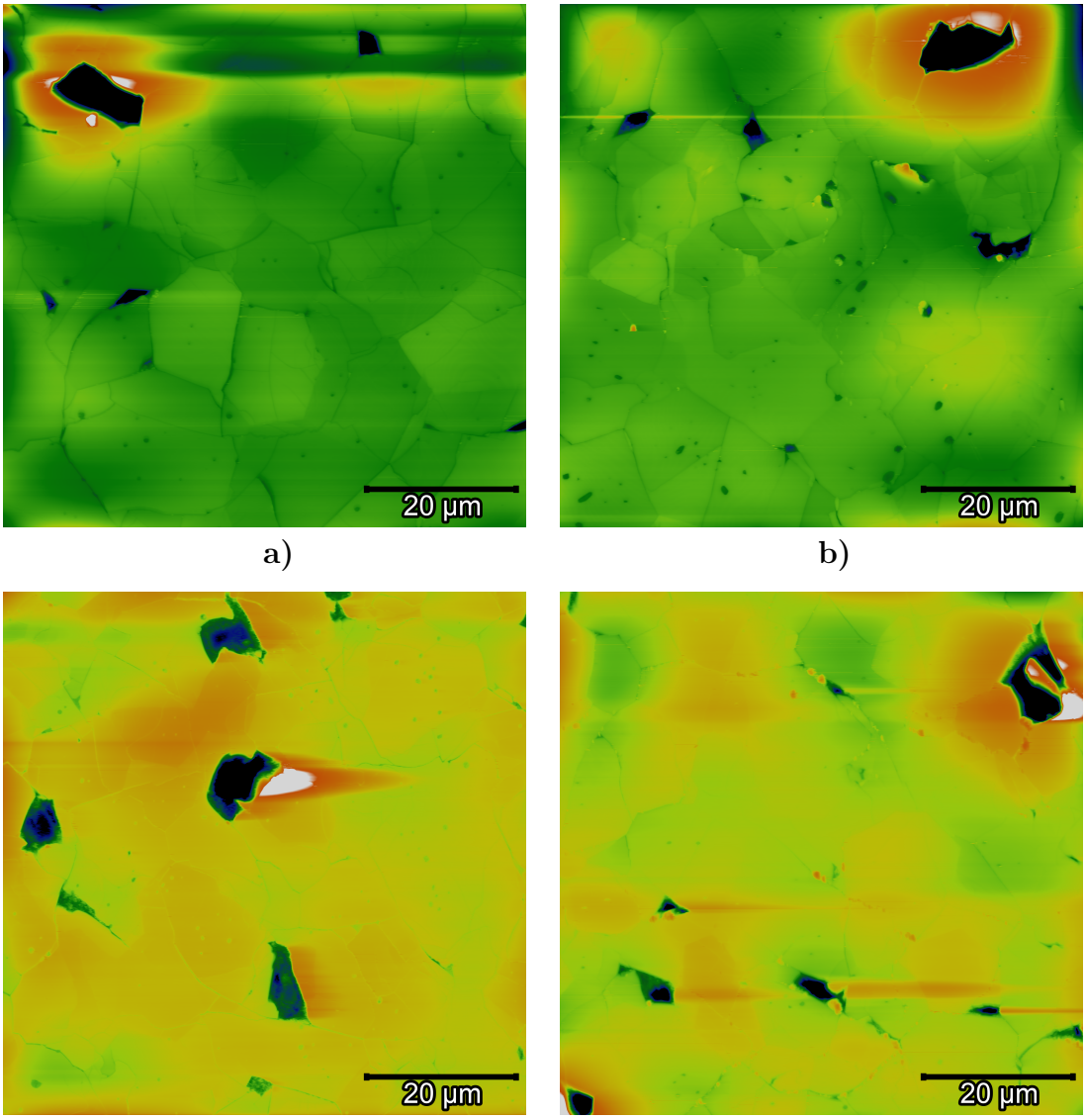

Fig. A.1.: Topography of $ErMnO_3$ at different cooling rates over T_C: a) 10^{-2} K/min, b) 10^{-1} K/min, c) 10^{0} K/min, d) 10^{1} K/min. All samples show the features discussed in section 4.1: Dark spots correspond to pores in the sample, small specks are caused by dirt. The dark lines that are visible can either signal a grain boundary or a microcrack inside a grain. To differentiate between the two, further analysis of the domain structure or electron backscatter diffraction (EBSD) are necessary.

B. Domain structure

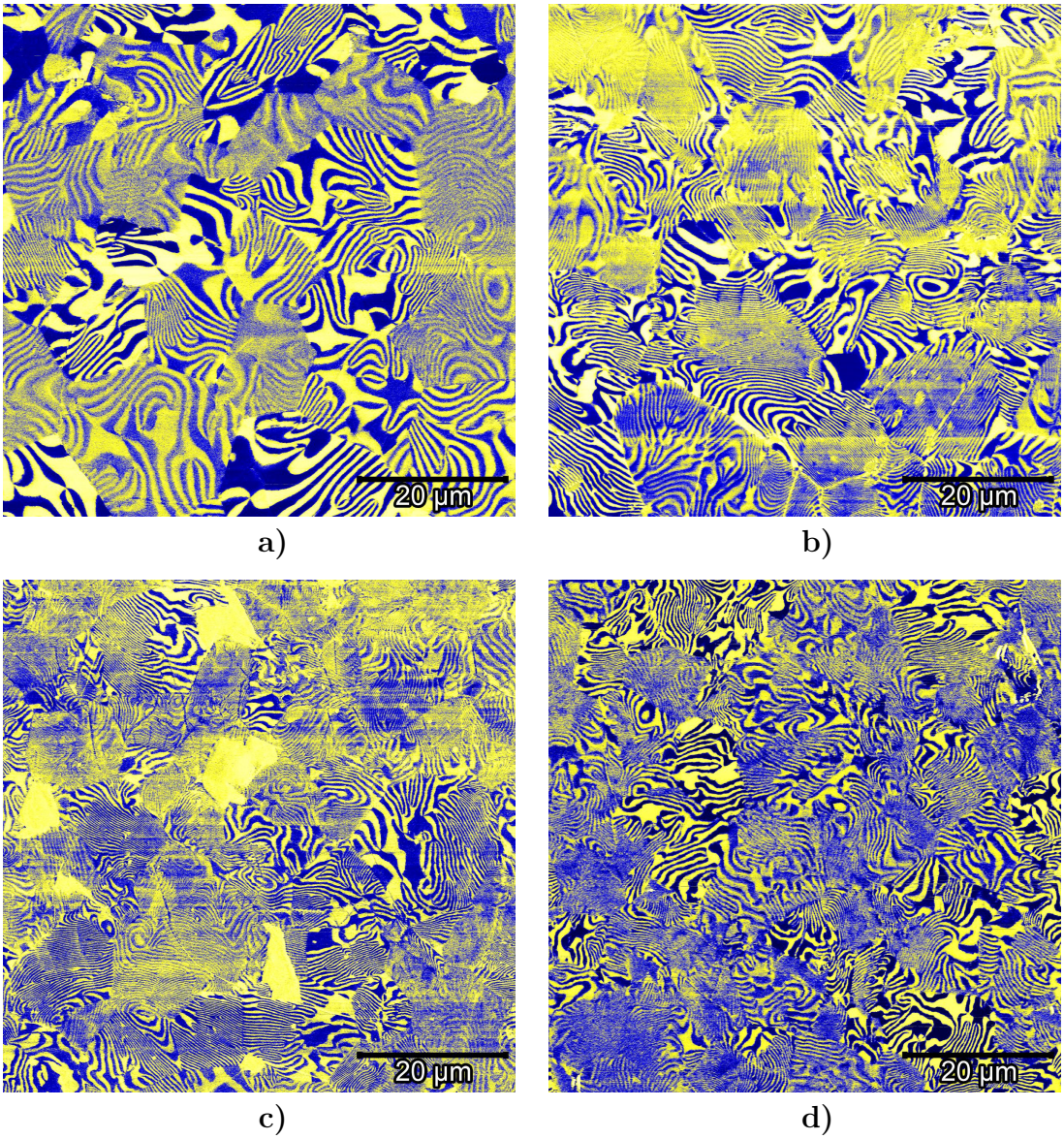

a) b) c) d)

Fig. B.1.: Domain structure of $ErMnO_3$ at different cooling rates over T_C: a) 10^{-2} K/min, b) 10^{-1} K/min, c) 10^{0} K/min, d) 10^{1} K/min. a)-c) show the lateral contrast while d) shows the normal contrast.